Aerodynamics Analysis of FX63-137 and LRN1015

Course: ENME 570/670

Instructor: Paul Ziade

Group 1:

Navid Moghtaderi	30050517
Joseph Isaak	30054923
Luis Sanabria	10114844
Karim Endrawes	30064229
Darius Clinton	10038177
Jay Kim	30042576

Due Date: Dec 8th, 2022

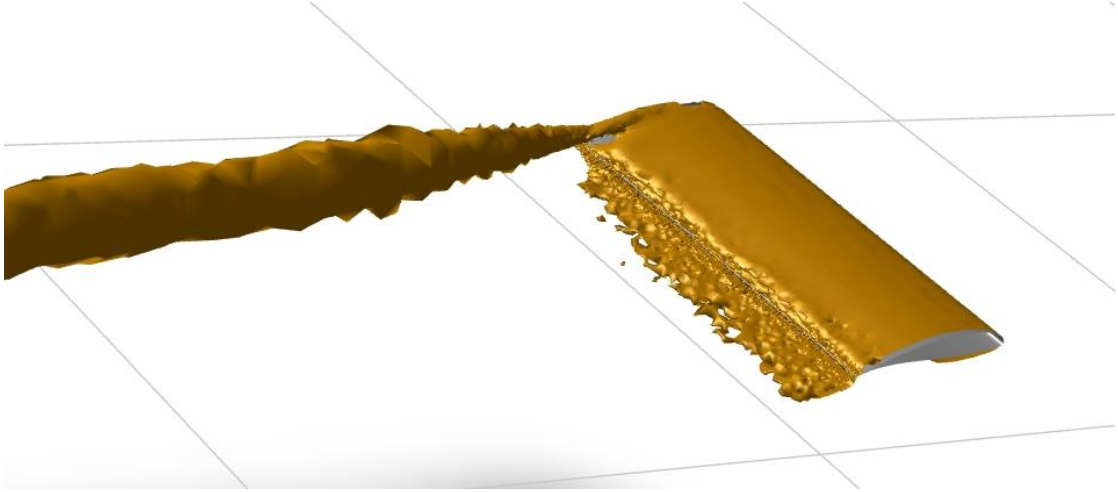

Abstract

This report details the analysis of two wings, the FX63-137 and LRN1015, comparing them against each other and evaluating their performance by virtue of their respective lift-to-drag ratios, stall angle behavior, and useful nature of volume. The purpose of this investigation is to judge the viability of these wings as candidates for a new unmanned aerial vehicle (UAV). These wings were first evaluated in 2D simulations where their performance metrics were subsequently determined using the Computational Fluid Dynamics (CFD) data. The better-performing wing was used to create a 3D wing and CFD form. The results of this investigation and the final determination for the most appropriate wing are described in terms of ratios of combined metrics.

Table of Contents

List of Figures

List of Tables

Introduction

The effectiveness of a wing is most often expressed in its lift to drag ratio which on a high level describes the wing's efficiency of translating thrust into lift. A high ratio of lift to drag would suggest that only a small amount of thrust is necessary for the wing to generate enough lift for it to be propelled through the air. Conversely, a low ratio of lift to drag would suggest that a significant amount of thrust is necessary for the wing to generate enough lift to be propelled through the air. In this project we are interested in selecting a high-performing wing for a new unmanned aerial vehicle considering its effectiveness, stall angle behaviour, and overall dimensions to arrive at an ideal geometry. Through research we identified two wings of interest that may satisfy our requirements, the FX63-137 and the LRN1015. Based on [3], the FX63-137 wing maximizes lift in low Reynolds flow with favourable stall angle behaviour, whereas the LRN1015 maximizes lift in high Reynolds flow and is currently installed on the world's most cutting-edge UAV, the Global Hawk. In order to compare these two wings toe-to-toe their expected behaviour in 2D CFD software is first observed to develop their theoretical performance metrics. The better performing wing is then used to develop a 3D physical model for wind-tunnel testing and 3D CFD analysis.

Background and Literature Review

Since humanity was first able to take to the skies there has been significant interest in perfecting wing technology. Governed by the non-linear and analytical solution-based Navier-Stokes equations, fluid flow phenomena has historically been difficult, if not near impossible, to compute and would require the expensive physical construction of wings to test and explore new designs. Through the development of wind-tunnel testing the cost and consequences of building full-scale test wings were able to be mitigated by only requiring a scaled down model to be constructed in order to validate models. This form of experimentation was incredibly beneficial as a small-scale test wing could be subjected to operating conditions to evaluate its coefficients of lift and drag and stall angle behaviour. With the introduction of computational power into the study of fluid dynamics, we have been able to develop investigative tools into the behaviour of wings allowing us to accurately predict their behaviour without the need to physically construct them. Though CFD has not been perfected and is still a very active area of research, there exists approximations today that aid in the determination of suitable planforms. The benefit of CFD analysis in comparison to experimentation arises from its cost effectiveness and ability to manipulate and determine all flow variables which would be impossible otherwise. The issues with CFD begin to arise in the simplifying assumptions that are made in order to make computation possible which can result in compounding error and unrealistic behaviour. Ultimately, the quality of results from simulation may only ever be as good as the quality of information input. Thus, there is still significant reliance on wind-tunnel testing to truly validate a model.

The guiding principle of our research was to find an airfoil with a proven high lift to drag ratio that would have favourable stall behaviour for the implementation on a new UAV. We have found the experimental performance of the FX 63-137 and LRN1015 to be the best performing

airfoils that suit our purposes. The FX 63-137 was demonstrated to be an excellent performer in low Reynolds flow, achieving a maximum lift coefficient near 1.7 with Reynolds number of 100,000 and maintained a positive lift coefficient for angles of attack ranging from -2° to 12° [3].

The LRN1015 proved to be the more appropriate option for higher Reynolds flow and is currently used on the Northrop Grumman RQ-4 Global Hawk, one of the most impressive UAVs to date. The design of the LRN1015 intends for the achievement of a lift coefficient of 1.0 in Mach 0.55 and Reynolds number 500,000. In experimentation this airfoil could generate a lift coefficient of 0.639 in these conditions, but, at Reynolds number 2,000,000 the wing could generate a lift coefficient of 1.030 [4].

Objective and Hypothesis Formulation

This experiment involved designing, testing, and manufacturing a high-performance wing for a new unmanned aerial vehicle. Based on aerodynamic theory, high lift to drag ratio wings (FX63-137) require less thrust than lower lift to drag ratio wings (LRN-1015) as it takes less of a pressure difference to get the former wing in the air. For any given value of lift, the angle of attack differs with varying speeds, hence the need for wind tunnel testing to see how a certain wing profile behaves when subjected to diverse pressure distributions. Typically, in the aerospace industry, designers will choose a wing which produces a lift to drag peak at the chosen cruising speed for an aircraft. By working backwards and preselecting the cruising speed for a given aircraft, designers are limited in choosing a wing design that specifies certain criteria and must conduct extensive calculations before the manufacturing of the wing can occur. The following figures illustrate airfoil terminology and the forces that act on an elemental area of it.

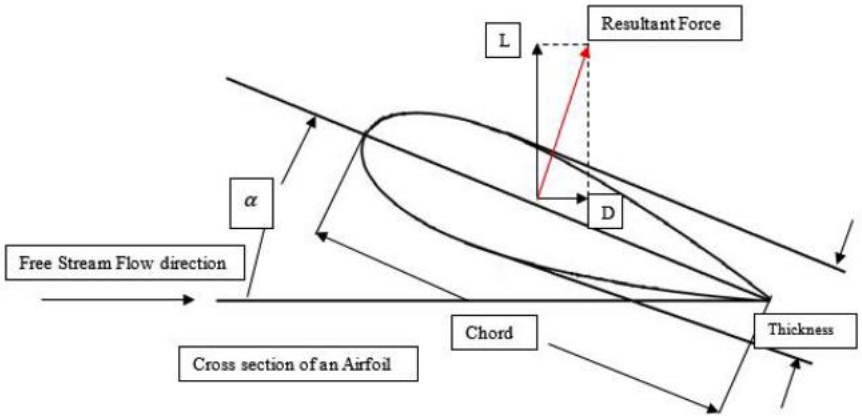

Figure 1: Airfoil Terminology [2]

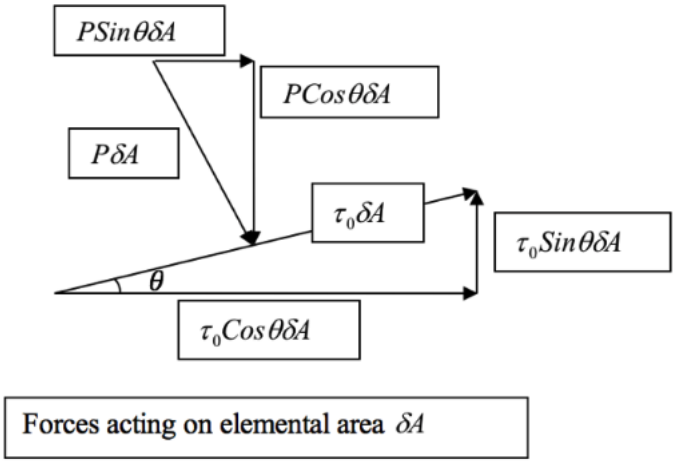

Figure 2: Forces Acting on An Airfoil [2]

where:

δA = Area of an Elemental portion of wing surface

θ = Local angle of inclination (AoA) of δA to the free stream flow direction

P = Local Pressure acting on δA

τ_0 = Local shear stress action on δA

U_∞ = Free stream velocity

q_∞ = Free stream dynamic head = $\frac{\rho U_\infty^2}{2}$

The drag and lift forces can be calculated respectively by:

$$D = \oint_S P \sin\theta \; dA + \oint_S \tau_0 \cos\theta \; dA$$

$$L = \oint_S P \cos\theta \; dA - \oint_S \tau_0 \sin\theta \; dA$$

where $\oint_S (\cdot)$ is the closed contour integral over the wetted surface of the body.

From the above, coefficients of lift and drag can be calculated as they are defined:

$C_L \equiv \frac{L}{qA}$ and $C_D \equiv \frac{D}{qA}$

where A is defined as the planform area (projected area of the body).

Based on the following, the first term in the drag force equation is the pressure drag (AKA form drag) while the second term is the frictional drag due to the shearing of the fluid flowing over the airfoil. The first term in the lift force equation is the lift due to the pressure distribution around the airfoil while the second term is the contribution to lift due to the skin friction of the wing. The latter is often neglected as it is very small compared to the first term when it comes to calculating lift force. It is evident from the equations that airfoil lift depends on many factors including but not limited to the geometry of the airfoil, angle of inclination, magnitude of free stream velocity, air density/viscosity, and compressibility.

Equipped with this knowledge, and assuming that free stream velocity, angle of attack range, Reynold's number flow, and compressibility is the same for both the FX63-137 and the LRN-1015 airfoils we are expecting to see a higher lift to drag ratio for the FX63-137 airfoil due to its geometry, with a slight drop in the lift to drag ratio when doing a 3D simulation due to the effects of downwash.

Methodology

A: CFD Methodology

The first step in conducting the CFD is to conduct a domain size analysis to ensure that the bounds of our domain aren't influencing or skewing the data in any way. This is done by keeping the mesh element size constant and creating different cases of domain sizes till convergence of C_l and C_d is observed. After domain size analysis is complete, and a favourable domain is selected, mesh refinement was conducted for 7 mesh resolutions ranging from a very coarse to a very fine mesh, again tracking the values of C_l and C_d for convergence. Once both the domain and mesh were set, the CFD simulations were able to begin. Firstly, a 2D case was simulated with angles of attacks ranging from -16° to 22° with an increment of +2° followed by a 3D simulation ranging from -8° to 8° again incremented at 2° each step.

B: Wind Tunnel Testing Methodology

The airfoils selected were modeled in SolidWorks. Each wing was modeled in sections so that they would meet the dimensional constraints of the 3D printer. The printer used for the project was the Prusa i3 MK3s. After the wings were printed, it was noted that the trailing edge did not print correctly on both wings. To repair the wings and ensure that these flaws did not impact the test results, J-B Weld epoxy was used to repair the trailing edge of the wings, as shown in Figure 3.

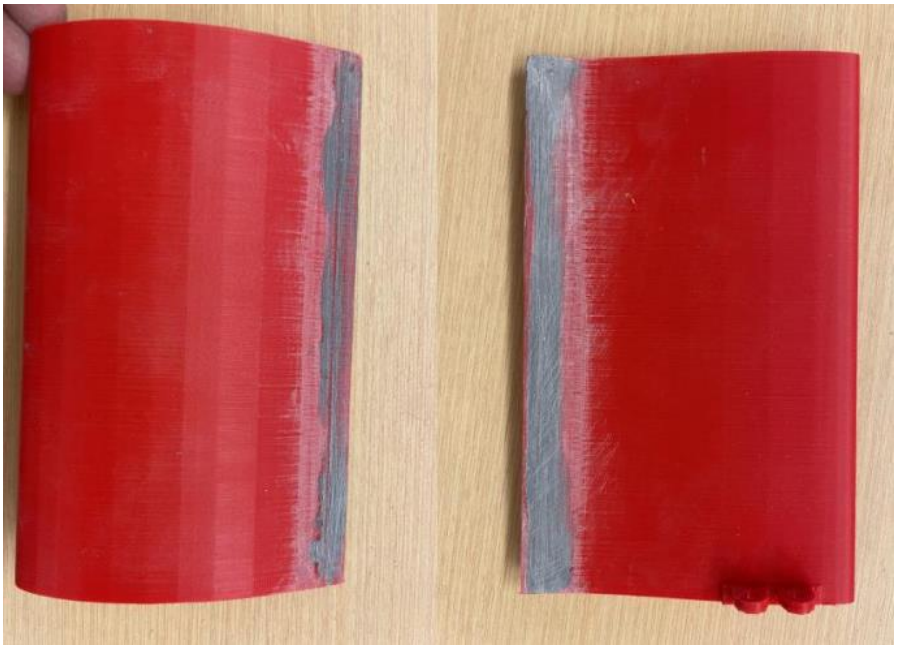

Figure 3: 3D Printed Airfoil Sections for the Rectangular Wing

Once the epoxy had set, the trailing edge was sanded down to its approximate airfoil shape. After the sanding was complete the two halves of the wing were glued together using super glue. Lastly, to maximize the experimental results, the 3D printed wings were wrapped with a polypropylene tape, more commonly known as “Tuck Tape”, as shown in Figure 4. The Tuck Tape was used to create a smoother surface in order to reduce skin friction drag compared to the unfinished 3D printed wing.

Figure 4: Completed Wings for Wind Tunnel Testing

Something to note was that given the geometry of the elliptical wing, it proved difficult to prevent the tape from wrinkling and creasing, especially around the rounded ends. However, the creases that were made were directed so that they were inline with the flow direction so as to minimize their effects on the flow. In this manner, it is expected that the creases would have negligible effects on the results.

The wind tunnel testing is mostly done automatically, with the user only needing to complete setup tasks at first. In order to start collecting data, the power supply to the wind tunnel must be on and allowed some time for the sensor to warm up in order to reduce error and increase the measurement accuracy. Once the sensor has had time to warm up, the airfoil is installed onto the force transducer at the quarter chord location ($c/4$) of the airfoil which is defined as the aerodynamic center. After installation, ensure that the airfoil is tightly attached to the force transducer and launch the Arduino IDE and serial monitor by clicking the magnifying glass symbol at the top right of the Arduino window. As well as launching the serial monitor, be sure to launch the sensor program and click log data in the top left of the window once ready to start logging datapoints. Before the test can run, it is important to home the airfoil by sending ‘h’ into the Arduino serial monitor and set the airfoil AoA to 0° by selecting ‘Bias’ in the sensor program. Once set, the wind tunnel can be turned on and left for a few minutes to reach a free

stream speed of $18.2m/s$. After a few minutes, send 'r' into the serial monitor and then "Collect Streaming" on the pop-up prompt. The remainder of the wind tunnel testing is completed automatically using the Arduino IDE and sensor application, and data will automatically be written into a .csv file and saved to the specified location. Once the angle of attack sweep has fully completed, ramp down the wind tunnel and then click "Stop Collecting" to complete the wind tunnel test. This process will automatically record data for varying angles of attack specified by the user at an interval of 2° per step while recording data for $20s$ at each interval.

Results

Computational Fluid Dynamics (CFD)

Computational fluid dynamics (CFD) was used to determine the aerodynamic metrics of the two airfoil profiles under consideration. Two-dimensional (2D) CFD models for both the FX63-137 and the LRN-1015 airfoils were performed. Once the metrics were obtained from the 2D CFD simulations the airfoil with the larger performance metric was selected to be tested in the wind tunnel. Furthermore, a 3D CFD simulation of this airfoil was also created.

In general, CFD is subdivided into three sections. The first section deals with constructing the mesh and is called preprocessing. The second section deals with running the simulation, and the last section deals with the results and is usually called postprocessing. To create the mesh for a CFD simulation two general steps must be taken. First, a domain size analysis must be conducted to make sure that the boundary conditions aren't influencing the results. Once the domain size is identified then a mesh refinement analysis must be performed.

To perform the domain size analysis five domains with different sizes were selected. To make sure that domain size is the only parameter that could influence the results, the mesh resolution for all domains was kept constant. CFD simulations were conducted for each case and the C_l and C_d values were collected. These values were then plotted as a function of domain sizes. One could argue that as the C_l and C_d values approached a constant number asymptotically the domain influence on the results would be decreasing to a negligible value. Note that the C_l and C_d values obtained during the domain size tests are not the correct values. They are just numerical values that are being tracked during the test. To obtain the correct lift and drag coefficient one must perform a mesh refinement analysis and model the boundary layer profiles too.

The mesh refinement analysis follows the same process as that of domain size analysis. Instead of changing the domain size, the element size is reduced. Seven different mesh resolutions are tested for each case and the C_l and C_d values are tracked and plotted as a function of mesh elements. Note that as C_l and C_d values approach a constant value asymptotically the mesh resolution impact on the results becomes negligible.

Wall functions were used to model the boundary layer for all CFD simulations. To calculate the Y^+ value, flat plate approximations were used to model the boundary layer near the airfoil. By definition Y^+ has the following equation:

$$Y^+ = \frac{U_\tau \Delta y \rho_\infty}{\mu_\infty}$$

Where ρ_∞ and μ_∞ are the freestream density and dynamic viscosity respectively and Δy is the first layer cell height. Note that the friction velocity can be defined as:

$$U_\tau = \sqrt{\frac{\tau_w}{\rho_\infty}}$$

The wall shear stress term was modeled using the following equation:

$$\tau_w = 0.5 C_f \rho_\infty u_\infty^2$$

Where u_∞ is the freestream velocity and C_f is the skin friction which is modeled using the following equation:

$$C_f = \frac{0.074}{Re^{\frac{1}{5}}}$$

A unit chord length was used to perform the CFD at Reynold's number of 10^5. Therefore, the velocity value was adjusted from $18.2\,\frac{m}{s}$ to $1.4710\,\frac{m}{s}$ to keep the Reynold's number fixed at 10^5. All fluid parameters used for CFD are listed in Table 1.

Table 1: Fluid parameters used during the CFD simulations

Parameters	Density, $\boldsymbol{\rho_\infty}[\frac{\boldsymbol{kg}}{\boldsymbol{m^3}}]$	Dynamic Viscosity, $\boldsymbol{\mu_\infty}[\frac{\boldsymbol{kg}}{\boldsymbol{ms}}]$	Chord Length, $\boldsymbol{C}$ $[\boldsymbol{m}]$	Velocity, $\boldsymbol{u_\infty}$ $[\frac{\boldsymbol{m}}{\boldsymbol{s}}]$
Values	1.225	1.805×10^{-5}	1.0	1.4710

Finally, $k-\varepsilon$ model was used to model the mean flow characteristics of the steady-state turbulent flow. The k$-\varepsilon$ model is a two-equation model that gives a general description of turbulence using two transport equations. One for the turbulent kinetic energy k and the second for the turbulent dissipation ε. The derivation of these equations is beyond the scope of this report, but the one-dimensional versions of these equations are shown below as an example.

The one-dimensional transport equation for turbulence kinetic energy is:

$$\rho \frac{\partial k}{\partial t} + \rho \bar{u}_j \frac{\partial k}{\partial x_j} = \frac{\partial}{\partial x_j}\left(\left(\mu + \frac{\mu_T}{\sigma_\varepsilon}\right)\frac{\partial k}{\partial x_j}\right) + \tau_{ij}^R \frac{\partial \bar{u}_i}{\partial x_j} - \rho\varepsilon$$

The one-dimensional transport equation for turbulence dissipation is:

$$\rho \frac{\partial \varepsilon}{\partial t} + \rho \bar{u}_j \frac{\partial \varepsilon}{\partial x_j} = \frac{\partial}{\partial x_j}\left(\left(\mu + \frac{\mu_T}{\sigma_\varepsilon}\right)\frac{\partial \varepsilon}{\partial x_j}\right) + C_{\varepsilon 1}\frac{\varepsilon}{k}\tau_{ij}^R \frac{\partial \bar{u}_i}{\partial x_j} - C_{\varepsilon 2}\frac{\rho\varepsilon^2}{k}$$

It is worth while mentioning that the $k-\varepsilon$ model does not perform well near walls and wall functions are needed to model the flow near walls. Using equations provided above a first layer height can be calculated for a $Y^+ = 60$. An example calculation is shown below:

$$C_f = \frac{0.074}{(100000)^{\left(\frac{1}{5}\right)}} = 7.4 \times 10^{-3}$$

$$\tau_w = (0.5)(7.4 \times 10^{-3})\left(1.225\frac{kg}{m^3}\right)\left(1.4710\frac{m}{s}\right) = 9.807 \times 10^{-3}\ Pa$$

$$U_\tau = \sqrt{\frac{9.807 \times 10^{-3} Pa}{1.225\frac{kg}{m^3}}} = 0.08947\frac{m}{s}$$

Rearranging the Y^+ equation we get:

$$\Delta y\ = \frac{Y^+ \mu_\infty}{U_\tau \rho_\infty}$$

$$\Delta y\ = \frac{(60)(1.805\ \times 10^{-5}\frac{kg}{ms})}{(0.08947\frac{m}{s})(1.225\frac{kg}{m^3})} = 0.01\ m$$

The first cell height is set to $0.01\ m$ for all the CFD simulations.

The rest of this sections contains results in tables and figures for domain and mesh refinement analysis and obtained C_l and C_d data.

Two-Dimensional CFD Modeling for FX63-137

Table 2 lists the lift and drag coefficients calculated for domain size analysis of 2D FX63-137 airfoil. As one can see the value of lift and drag asymptoticly approach a constant number as the domain size increases. This information is plotted in Figure 5 and Figure 6, respectively. Table 3 lists the lift, drag and number of nodes used during the mesh refinement analysis for the 2D FX63-137 airfoil. As one can see the lift and drag values approach a constant number asymptoticly as the mesh resolution increases. This information is plotted in Figure 7 and Figure 8, respectively, as well. Finally, Table 4 is the list of all lift and drag coefficients obtained at different angles of attack for the CFD simulations of 2D FX63-137 airfoil. Values in Table 4 are used later to plot C_l and C_d curves as functions of angle of attack. This information can be found in the discussion section of the report.

Table 2: Lift and drag coefficients obtained for domain size analysis of 2D FX63-137 airfoil

Domain Size ID	Domain Size	Lift Coefficient, C_l	Drag Coefficient, C_d
1	Smallest	0.43065	0.034092
2	Small	0.43465	0.032363
3	Medium	0.43697	0.031434
4	Large	0.43864	0.030743
5	Largest	0.43993	0.030293

Table 3: Lift and drag coefficients obtained for mesh refinement analysis of 2D FX63-137 airfoil

Mesh Sizes	Coarsest	Coarse 1	Coarse 2	Medium	Fine 1	Fine 2	Finest
Node number	32530	58965	80575	119450	222885	303510	529810
Element Number	32200	58500	80000	118750	222000	302500	528500
Lift Coeff, C_l	0.6115	0.69082	0.72334	0.76297	0.79751	0.79959	0.78362
Drag Coeff, C_d	0.036749	0.03384	0.031929	0.030949	0.030353	0.029739	0.029183

Table 4: C_l and C_d obtained for 2D FX63-137 airfoil at different angles of attack

Angle of Attack, α [deg]	Lift Coefficient, C_l	Drag Coefficient, C_d	Lift/Drag Coeff, $\frac{C_l}{C_d}$
-16	-0.2543	0.1634	-1.5559
-14	-0.1657	0.1275	-1.2997
-12	-0.1516	0.1110	-1.3654
-10	-0.1445	0.0949	-1.5229
-8	-0.0913	0.0735	-1.2422
-6	0.0775	0.0486	1.5942
-4	0.3315	0.0320	10.3449
-2	0.5818	0.0271	21.4608
0	0.7995	0.0273	29.2747
2	0.9954	0.0308	32.3261
4	1.1626	0.0377	30.8284
6	1.2933	0.0482	26.8464
8	1.2933	0.0482	26.8464
10	1.4361	0.0886	16.2156
12	1.4032	0.1184	11.8504
14	1.3323	0.1524	8.7438
16	1.3359	0.2022	6.6058
18	1.3265	0.2535	5.2336
20	1.4114	0.3384	4.1709
22	1.4737	0.4187	3.5194

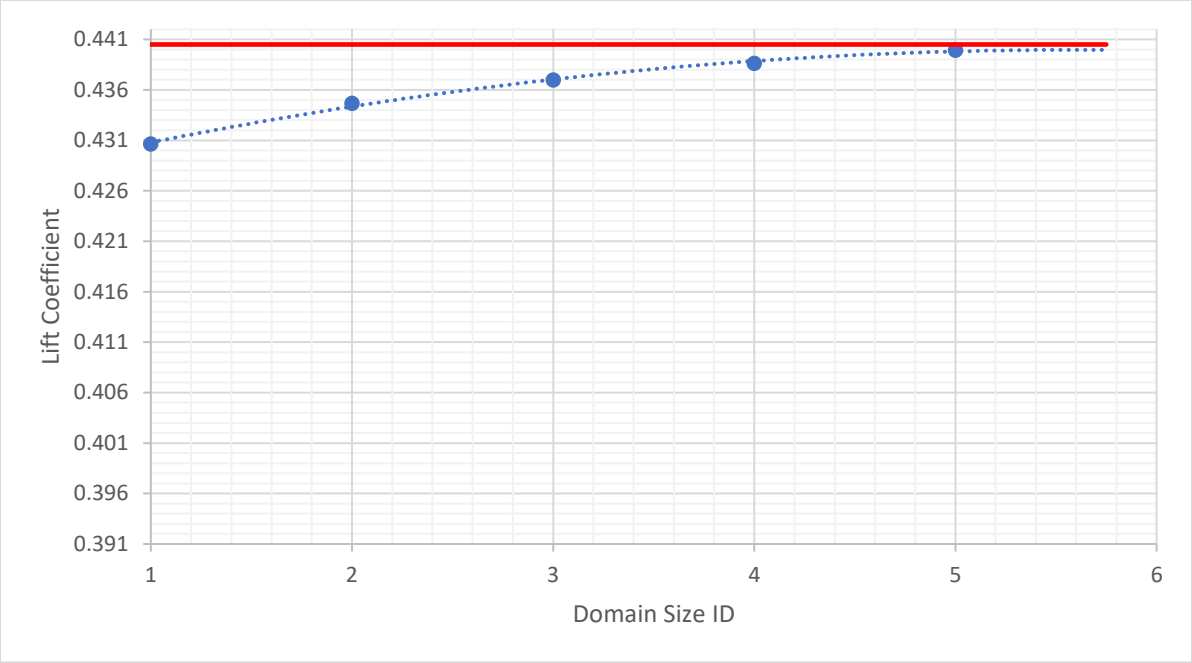

Figure 5: Lift coefficient as a function of domain size for the 2D FX63-137 CFD simulation.

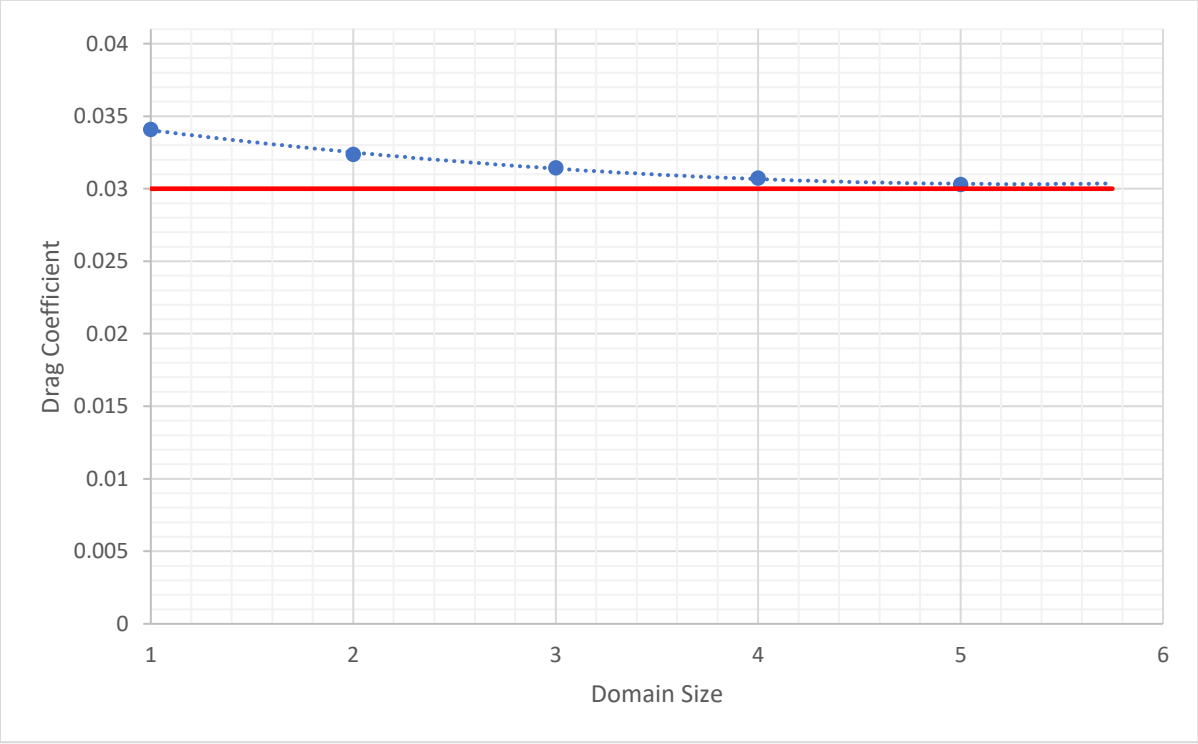

Figure 6: Drag coefficient as a function of domain size for the 2D FX63-137 CFD simulation.

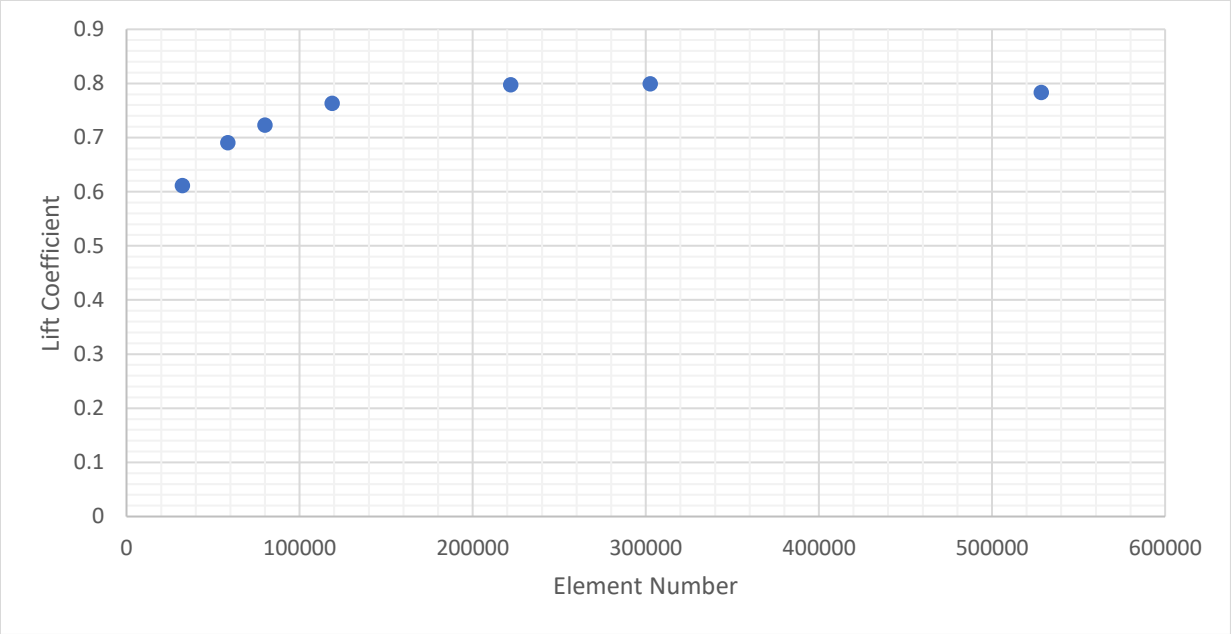

Figure 7: Life coefficient as a function of element number for 2D FX63-137 airfoil.

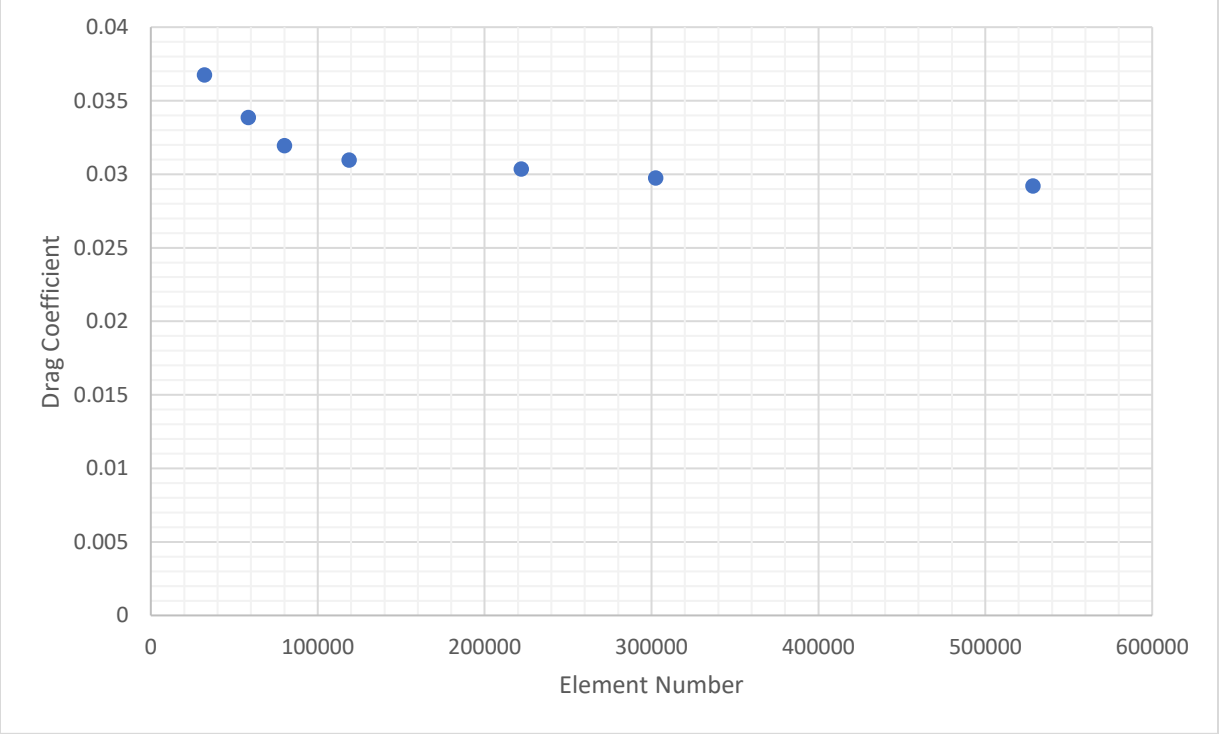

Figure 8: Drag coefficient as a function of element number for 2D FX63-137 airfoil

Two-Dimensional CFD Modeling for LRN-1015

Table 5 lists the lift and drag coefficients calculated for domain size analysis for 2D LRN-1015 airfoil. As one can see, the value of lift and drag asymptoticly approach a constant number as the domain size increases. This information is plotted on Figure 9 and Figure 10. Table 6 lists the lift, drag and number of nodes used during the mesh refinement analysis for the 2D LRN-1015

airfoil. As one can see the lift and drag values approach a constant number asymptoticly as the mesh resolution increases. This information is plotted in Figure 11 and Figure 12 as well.y Finally, Table 7 is the list of all lift and drag coefficients obtained at different angles of attack for the CFD simulations of 2D LRN-1015 airfoil. Values in Table 7 are used later to plot C_l and C_d curves as functions of angle of attack. This information can be found in the discussion section of the report.

Table 5: Lift and drag coefficients obtained for domain size analysis of 2D LRN-1015 airfoil

Domain Size ID	Domain Size	Lift Coefficient, $\boldsymbol{C_l}$	Drag Coefficient, $\boldsymbol{C_d}$
1	Smallest	0.30771	0.024826
2	Small	0.31032	0.02373
3	Medium	0.31166	0.023204
4	Large	0.31246	0.02284
5	Largest	0.31306	0.02261

Table 6: Lift and drag coefficients obtained for mesh refinement analysis of 2D LRN-1015 airfoil

Mesh Sizes	Coarsest	Coarse 1	Coarse 2	Medium	Fine 1	Fine 2	Finest
Node number	35906	66415	93255	137860	225775	312155	547450
Element Number	35600	66000	92750	137250	225000	311250	546250
Lift Coeff, $\boldsymbol{C_l}$	0.47423	0.49518	0.50679	0.50497	0.48413	0.48625	0.47861
Drag Coeff, $\boldsymbol{C_d}$	0.031043	0.028739	0.028833	0.028492	0.027375	0.027657	0.02763

Table 7: C_l and C_d obtained for 2D LRN-1015 airfoil at different angles of attack

Angle of Attack, $\boldsymbol{\alpha}$ $[\boldsymbol{deg}]$	Lift Coefficient, $\boldsymbol{C_l}$	Drag Coefficient, $\boldsymbol{C_d}$	Lift/Drag Coeff, $\frac{\boldsymbol{C_l}}{\boldsymbol{C_d}}$
-16	-0.5234	0.2555	-2.0488
-14	-0.3583	0.1795	-1.9962
-12	-0.2418	0.1177	-2.0549
-10	-0.3103	0.0836	-3.7107
-8	-0.2399	0.0575	-4.1695
-6	-0.1004	0.0416	-2.4120
-4	0.0806	0.0325	2.4828
-2	0.2762	0.0236	11.6938
0	0.4786	0.0276	17.3211
2	0.6763	0.0297	22.7491
4	0.8612	0.0340	25.3031
6	1.0297	0.0409	25.1921
8	1.1664	0.0506	23.0559
10	1.2664	0.0633	20.0180
12	1.3326	0.0793	16.8075

14	1.3569	0.0996	13.6225
16	1.3779	0.1286	10.7130
18	1.3972	0.1745	8.0087
20	1.4094	0.2482	5.6789
22	1.5882	0.4131	3.8449

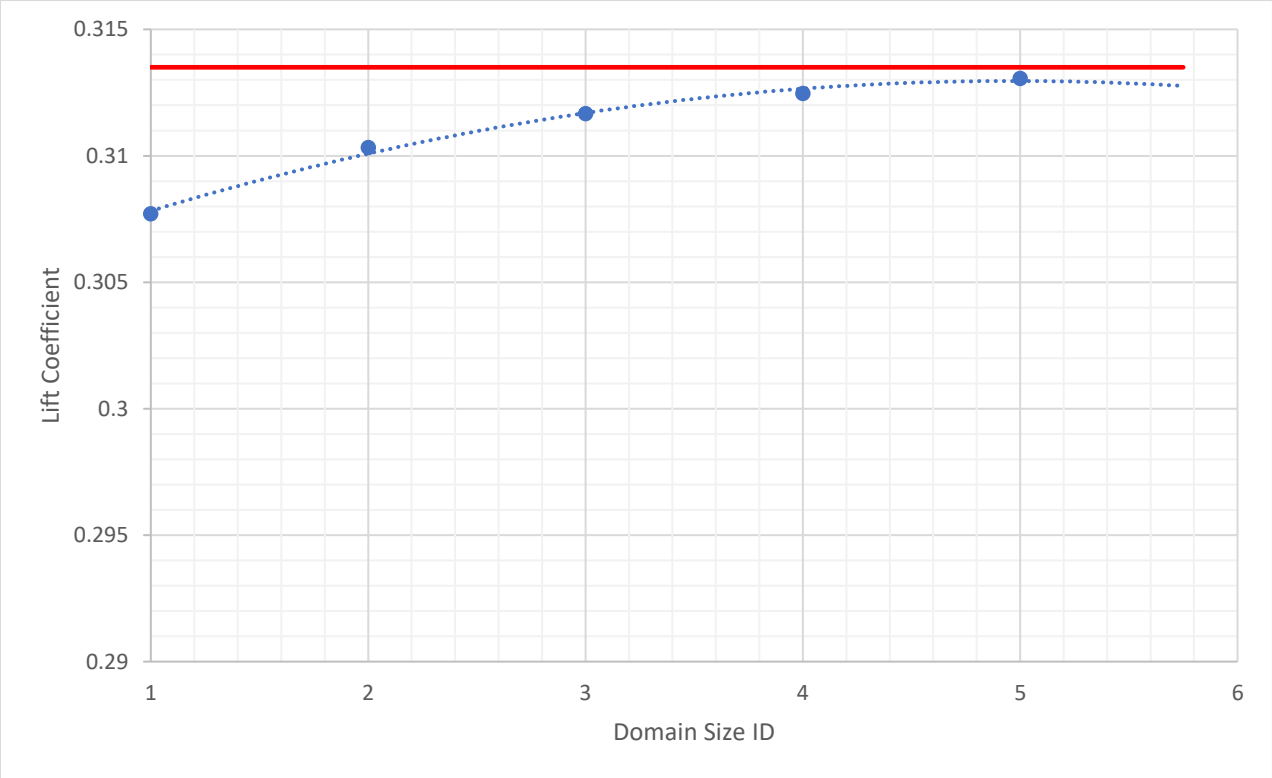

Figure 9: Lift coefficient as a function of domain size for the 2D LRN-1015 CFD simulation.

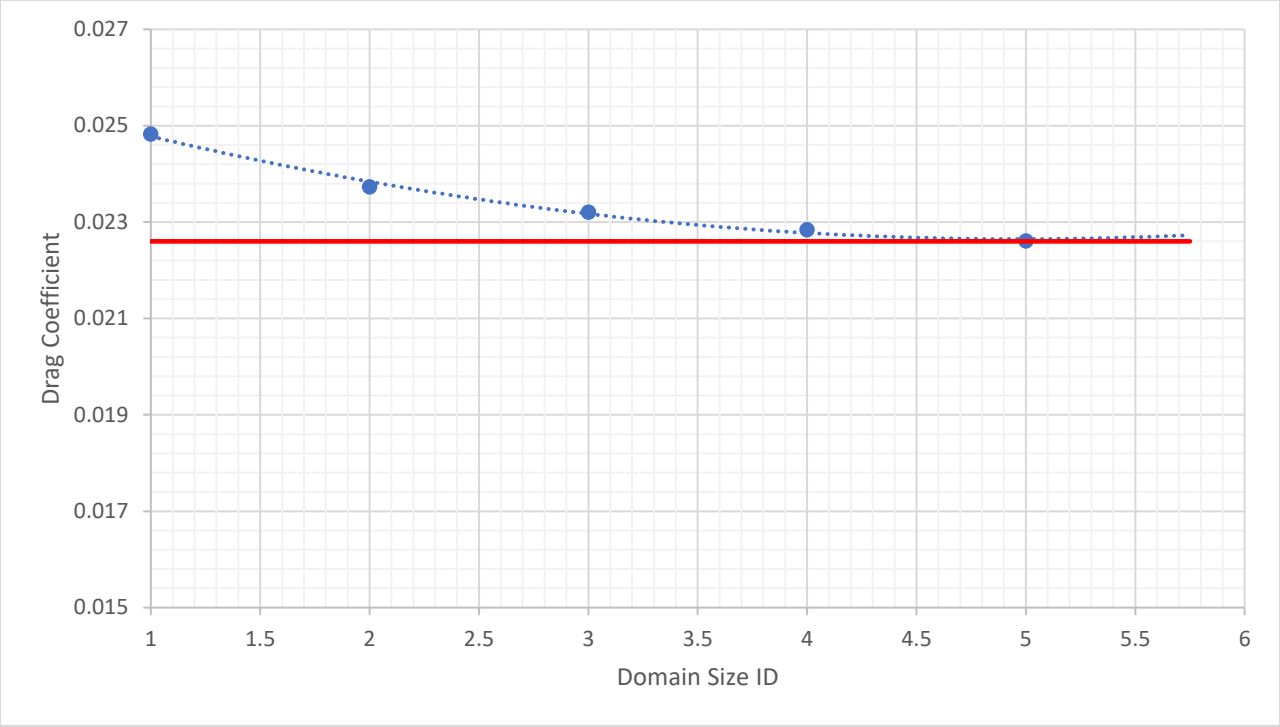

Figure 10: Drag coefficient as a function of domain size for the 2D LRN-1015 CFD simulation.

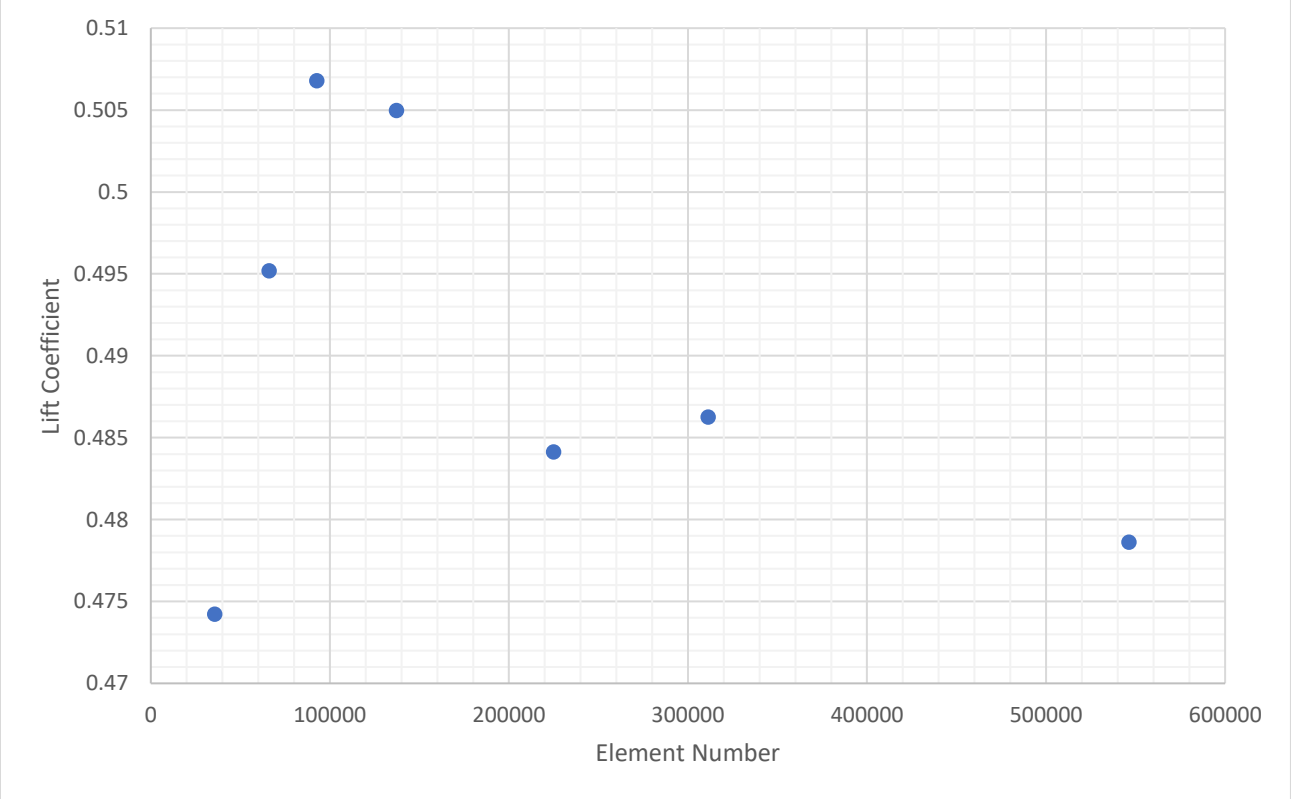

Figure 11: Life coefficient as a function of element number for 2D LRN-1015 airfoil.

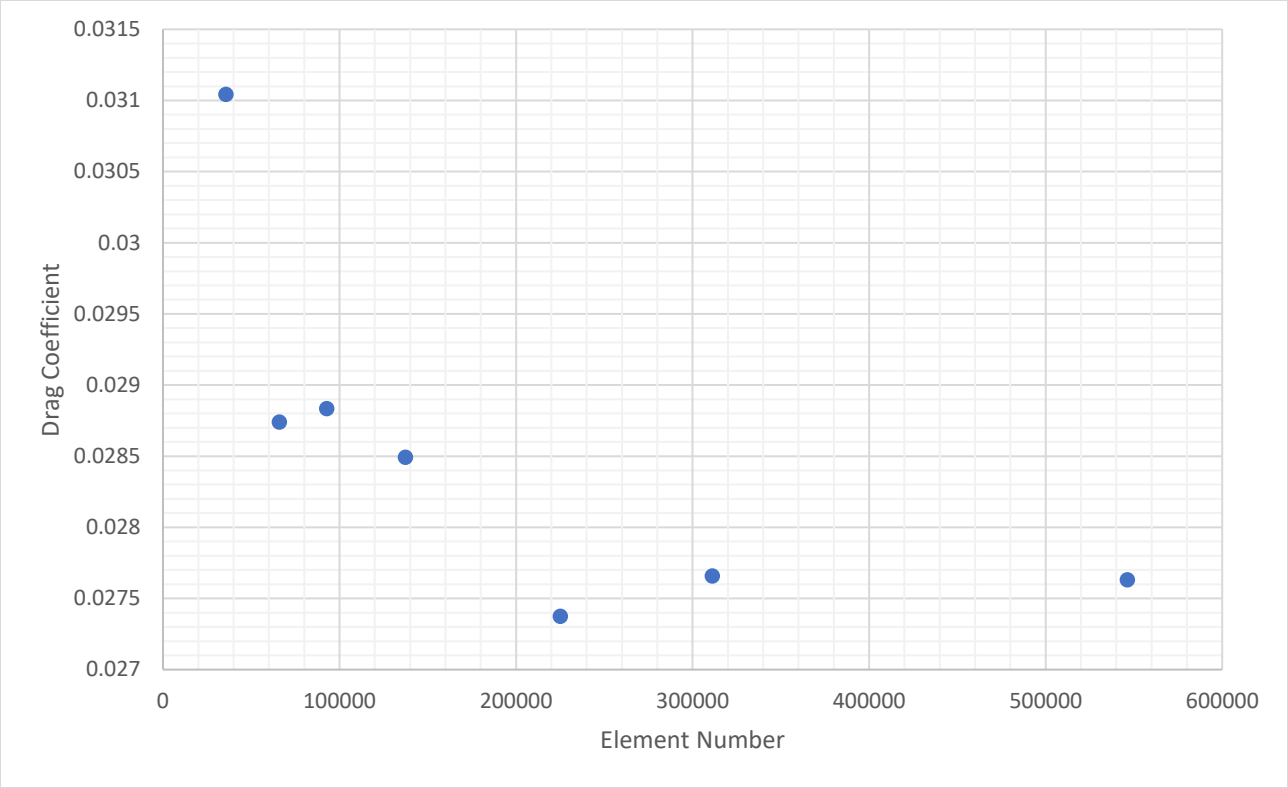

Figure 12: Drag coefficient as a function of element number for 2D LRN-1015 airfoil.

Three-Dimensional CFD Modeling

Table 8 lists the lift and drag coefficients calculated for domain size analysis for 3D FX63-137 airfoil. As one can see, the value of lift and drag asymptoticly approach a constant number as the domain size increases. This information is plotted in Figure 13 and Figure 14. Table 9 lists the lift, drag and number of nodes used during the mesh refinement analysis for the 3D FX63-137 airfoil. As one can see the lift and drag values do not approach a constant number as the mesh resolution increases. This suggests that the mesh needs to be more resolves. However, computers used to run the 3D CFD simulations did not have the computational capability to run CFD with more nodes. This information is plotted in Figure 15 and Figure 16 as well. Finally, Table 10 is the list of all lift and drag coefficients obtained at different angles of attack for the CFD simulations of 3D FX63-137 airfoil. Values in Table 10 are used later to plot C_l and C_d curves as functions of angle of attack. This information can be found in the discussion section of the report.

Table 8: Lift and drag coefficients obtained for domain size analysis of 3D FX63-137 wing CFD

Domain Size ID	Domain Size	Lift Coefficient, $\boldsymbol{C_l}$	Drag Coefficient, $\boldsymbol{C_d}$
1	Smallest	0.13337	0.029458
2	Small	0.12347	0.028523
3	Medium	0.12216	0.028416
4	Large	0.12044	0.028308
5	Largest	0.12146	0.028382

Table 9: Lift and drag coefficients obtained for mesh refinement analysis of 3D FX63-137 CFD

Mesh Sizes	Coarsest	Coarse 1	Coarse 2	Medium	Fine 1	Fine 2	Finest
Node number	42343	66543	107391	166519	239814	457068	581537
Element Number	187803	309245	517608	819249	1190203	2527320	3205583
Lift Coeff, C_l	0.11927	0.12138	0.12511	0.12581	0.12578	0.12686	0.12721
Drag Coeff, C_d	0.028299	0.028234	0.028075	0.027994	0.027818	0.028941	0.028566

Table 10: C_l and C_d obtained for 3D FX63-137 airfoil at different angles of attack

Angle of Attack, α [deg]	Lift Coefficient, C_l	Drag Coefficient, C_d	Lift/Drag Coeff, $\frac{C_l}{C_d}$
-8	0.3651	0.0043	84.0478
-6	0.4077	0.0119	34.1949
-4	0.4485	0.0221	20.2712
-2	0.4878	0.0348	14.0331
0	0.5257	0.0497	10.5811
2	0.5624	0.0668	8.4252
4	0.5979	0.0859	6.9594
6	0.6324	0.1070	5.9088
8	0.6665	0.1301	5.1230

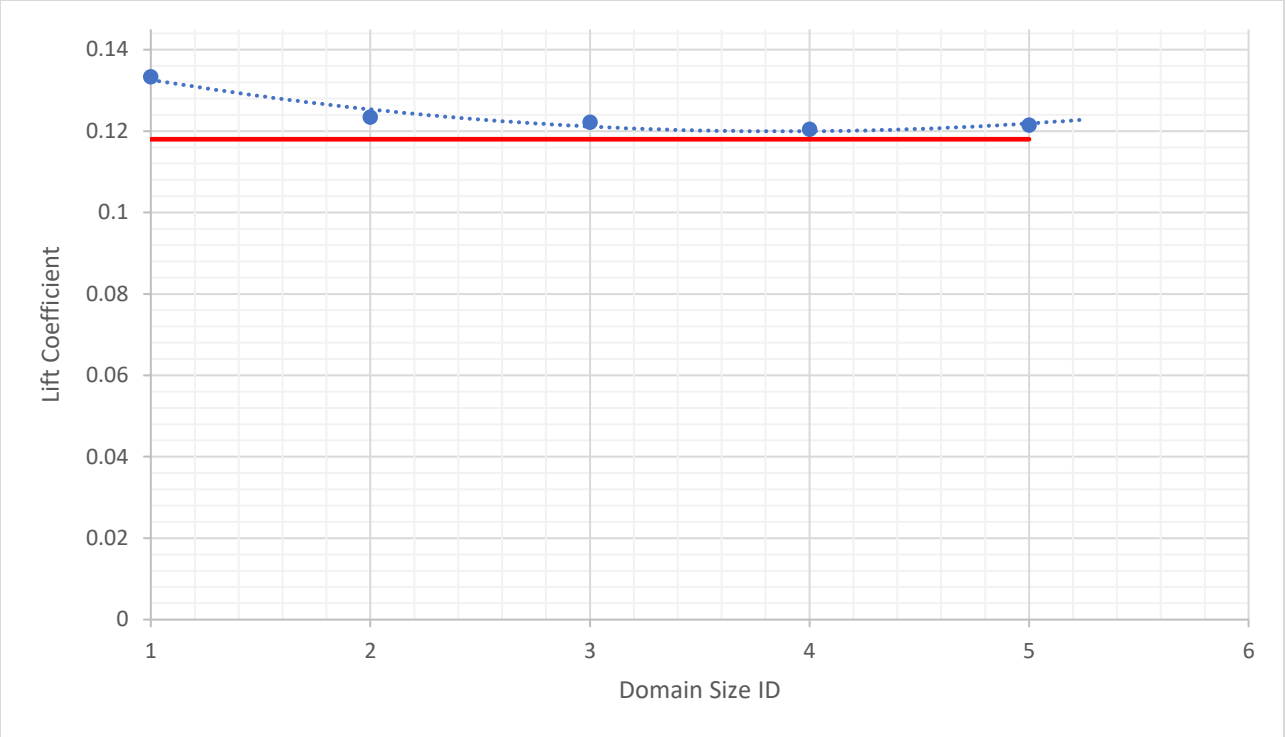

Figure 13: Lift coefficient as a function of domain size for the 3D FX63-137 CFD simulation.

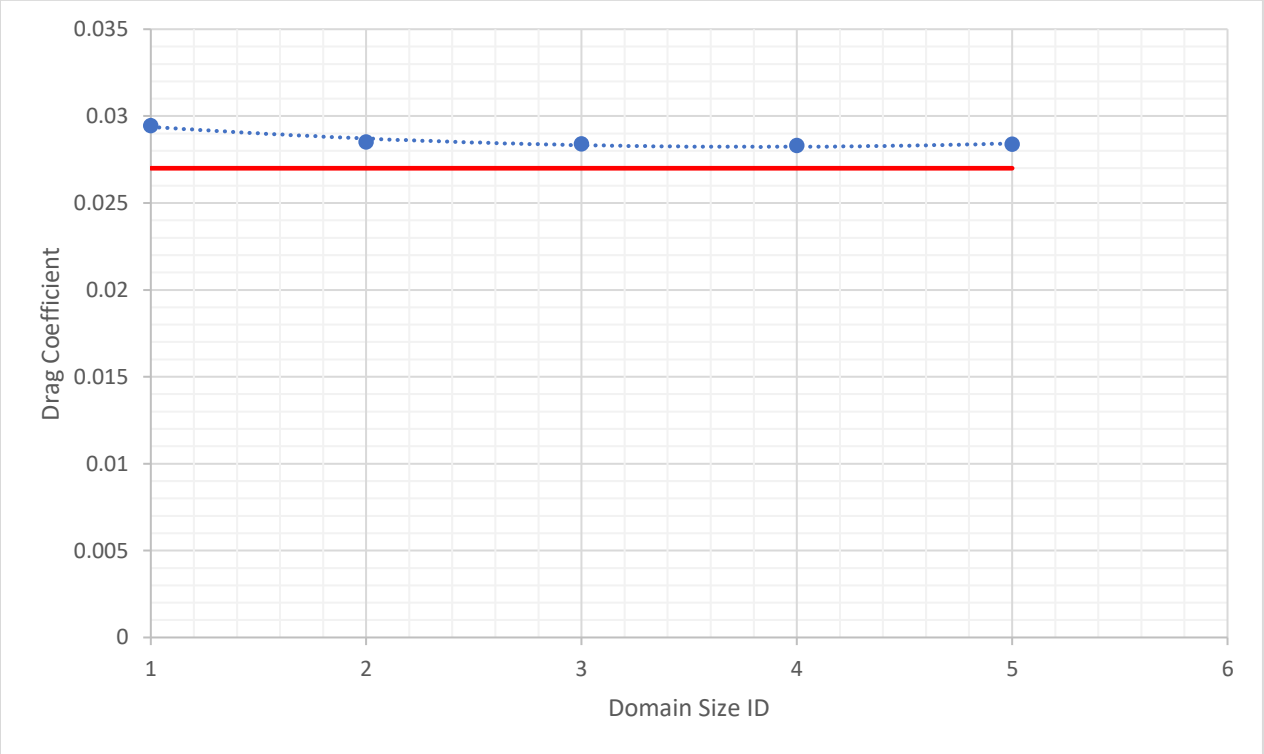

Figure 14: Drag coefficient as a function of domain size for the 3D FX63-137 CFD simulation.

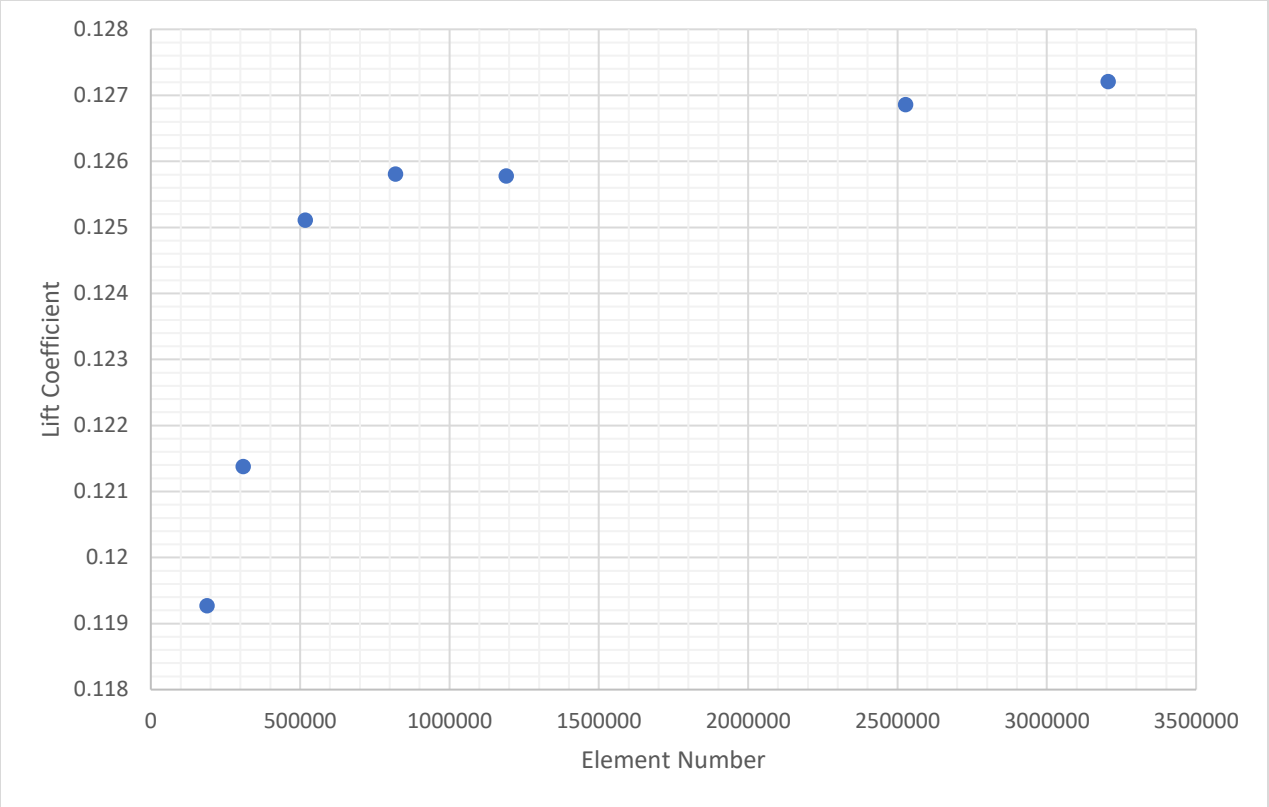

Figure 15: Life coefficient as a function of element number for 3D FX63-137 airfoil.

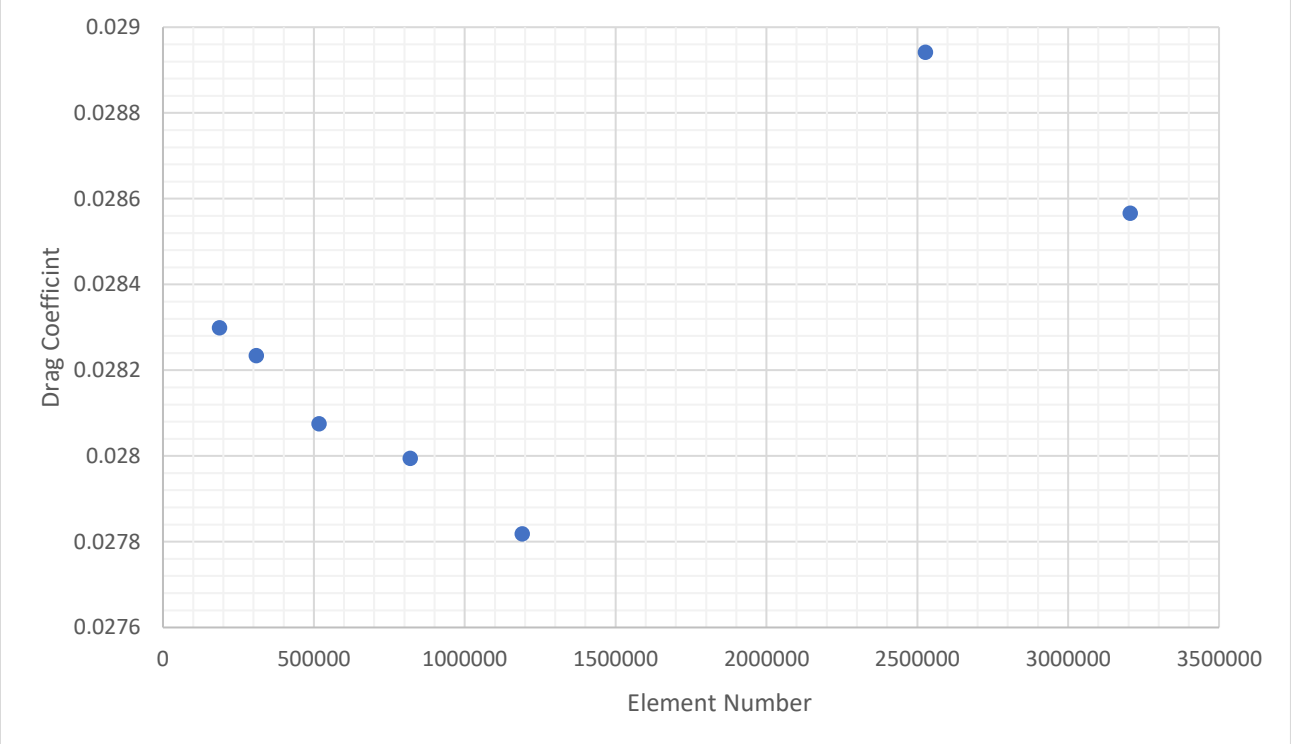

Figure 16: Drag coefficient as a function of element number for 3D FX63-137 airfoil

Wind tunnel Test Results

A 6-axis force transducer was used to measure the lift, drag and moment forces on the airfoil. These results were used to calculate non-dimensional parameters such as lift and drag coefficients. Table 11 lists the values of ambient pressure, density and temperature used during the operation of the wind tunnel. It is important to note that these values are assumed and were not measured directly during the lab.

Table 11: Air properties used during this experiment. [4]

Gas Constant $\boldsymbol{R}$ $[\frac{J}{Kmol}]$	Density, $\boldsymbol{\rho}$ $[\frac{kg}{m^3}]$	Pressure, $\boldsymbol{P_{atm}}$ $[\boldsymbol{Pa}]$	Temperature, $\boldsymbol{T}$ [℃]	Molar Mass $\boldsymbol{M}$ $[\frac{kg}{mol}]$
8.314	1.0563	89170.00	21	0.02897

The destiny was calculated using the ideal gas law. The sample calculation is shown below:

$$\rho_\infty = \frac{MP}{RT}$$

Plugging values would yield:

$$\rho_\infty = \frac{(0.02897\ \frac{kg}{mol})(89170.00\ Pa)}{(8.314\ \frac{J}{Kmol})(21 + 273.15)K} = 1.0563\frac{kg}{m^3}$$

The wing tested was a FX63-137 with elliptical planform area. To collect the force data, each angle of attack is held for 20 seconds, and the force data is collected at a frequency of 125 Hz. This implies that for each angle of attach there is 2500 force data points. To conduct the analysis the mean of these data points at each angle of attack was calculated and reported in Table 12. Note that the actual mean calculations are shown in the analysis section of this report. Based on the way the force transducer is connected to the airfoil, the X axis which is the axis that is in line with the lift force is inverted. So, to obtain the correct lift force all lift data is multiplied by -1. Furthermore, the Y axis is tangent to the freestream direction and the Z axis is orthogonal to the freestream direction.

Table 12: Mean force and moment data obtained for FX63-137 wing

$\boldsymbol{F_x}, [\boldsymbol{N}]$	$\boldsymbol{F_y}, [\boldsymbol{N}]$	$\boldsymbol{F_z}, [\boldsymbol{N}]$	$\boldsymbol{M_x}[\boldsymbol{Nm}]$	$\boldsymbol{M_y}[\boldsymbol{Nm}]$	$\boldsymbol{M_z}[\boldsymbol{Nm}]$
1.7673	0.1312	1.1925	-0.0139	-0.0997	-0.0382
1.4192	0.1236	1.1687	-0.0138	-0.0755	-0.0341
1.0136	0.1205	1.1495	-0.0143	-0.0486	-0.0349
0.6695	0.1313	1.1125	-0.0152	-0.0248	-0.0413
0.3228	0.1658	1.0763	-0.0172	-0.0031	-0.0548
-0.0138	0.2346	1.0315	-0.0211	0.0200	-0.0842
-0.2393	0.3195	0.9645	-0.0258	0.0347	-0.1209
-0.3739	0.3898	0.9388	-0.0298	0.0436	-0.1496
-0.2757	0.4390	0.9546	-0.0353	0.0619	-0.1701
1.7559	0.1064	0.7682	-0.0141	-0.0926	-0.0394

2.0758	0.1214	0.6861	-0.0149	-0.1133	-0.0457
2.3912	0.1428	0.6168	-0.0162	-0.1338	-0.0545
2.7095	0.1696	0.5564	-0.0180	-0.1537	-0.0657
2.9652	0.1967	0.5357	-0.0194	-0.1716	-0.0767
3.2702	0.2345	0.5195	-0.0216	-0.1890	-0.0916
3.5010	0.2837	0.4997	-0.0245	-0.2044	-0.1076
3.6622	0.3372	0.5026	-0.0275	-0.2157	-0.1264
3.7168	0.3977	0.5196	-0.0311	-0.2197	-0.1475
1.5580	0.0602	0.6277	-0.0129	-0.0713	-0.0338

Discussion

CFD Simulations

Aerodynamic Force Coefficients

As was mentioned before domain size analysis and mesh refinement tests were conducted for each CFD simulation. Based on the test's performance and the results presented in figuresFigure 5 through 16Figure 16, the "*largest*" domain size was selected for the CFD simulations. Moreover, the "*finest*" mesh was selected, and the boundary layer was modeled with a Y^+ of 60. It is worth noting that the mesh refinement process for the 3D FX63-137 wing simulation was incomplete. This was due to lack of computational power that was needed to resolve the large 3D space with nodes.

The lift and drag coefficients for the 2D and 3D FX63-137 CFD simulations are plotted in Figure 20 and Figure 25, respectively. As one can see, the 2D FX63-137 airfoil has a larger lift value at each angle of attack when it is compared to its 3D equivalent. For example, at zero degrees the 2D lift coefficient is $C_l = 0.7995$, while the 3D FX63-137 wing is generating a $C_L = 0.5257$. This is due to downwash which reduces the angle of attack that the wing is creating relative to freestream velocity. Due to downwash, there is a net downward velocity which forces the mean freestream velocity vector to point downwards. Therefore, the wing only sees the effective angle of attack which is defined as $\alpha_{eff} = \alpha_{geo} - \alpha_i$ and not the geometric angle of attack. Moreover, due to downwash there is an extra component of drag known as induced drag. The induced drag increases the drag coefficient of the 3D wing when it is compared to its 2D counterpart. For example, at the zero angle of attack the FX63-137 wing generates approximately a drag coefficient of $C_D = 0.0497$ while the 2D airfoil generates only $C_d = 0.0273$.

Note that the slope of the C_l curve is mostly constant for small angles of attack. This indicates that as angle of attack changes the lift coefficient changes linearly with a slope of 0.1031 . The slope of C_L curve starts to decrease significantly at an angle of attack of $\alpha = 14^{\circ}$. This is most likely due to flow separation. However, the lift coefficient starts to increase after the C_l value has gone over $\alpha = 16^{\circ}$. This could be due to formation of a bubble and is investigated more in depth later. The stall angle cannot be determined from the CFD experiment, but it was assumed to be $\alpha = 14^{\circ}$. The stall angle and lift slope are listed in Table 13 below. Lastly, the largest $\frac{C_l}{C_d}$ value is

32.33 and is obtained at an angle of attack of 2°. This can be observed in Figure 19 as well. This implies that the 2°AoA is the most optimal angle of attack as it generates the maximum lift for a given amount of drag.

Table 13: Stall angle, Lift slope and optimal angle of attack for FX63-137 (2D CFD)

Stall Angle $\boldsymbol{\alpha_{stall}}$ $[\boldsymbol{deg}]$	Lift Slope $[\frac{\mathbf{1}}{\boldsymbol{deg}}]$	Largest $\frac{\boldsymbol{C_l}}{\boldsymbol{C_d}}$	Largest $\frac{\boldsymbol{C_l}}{\boldsymbol{C_d}}$ angle $[\boldsymbol{deg}]$
14.0	0.1031	32.33	2.0

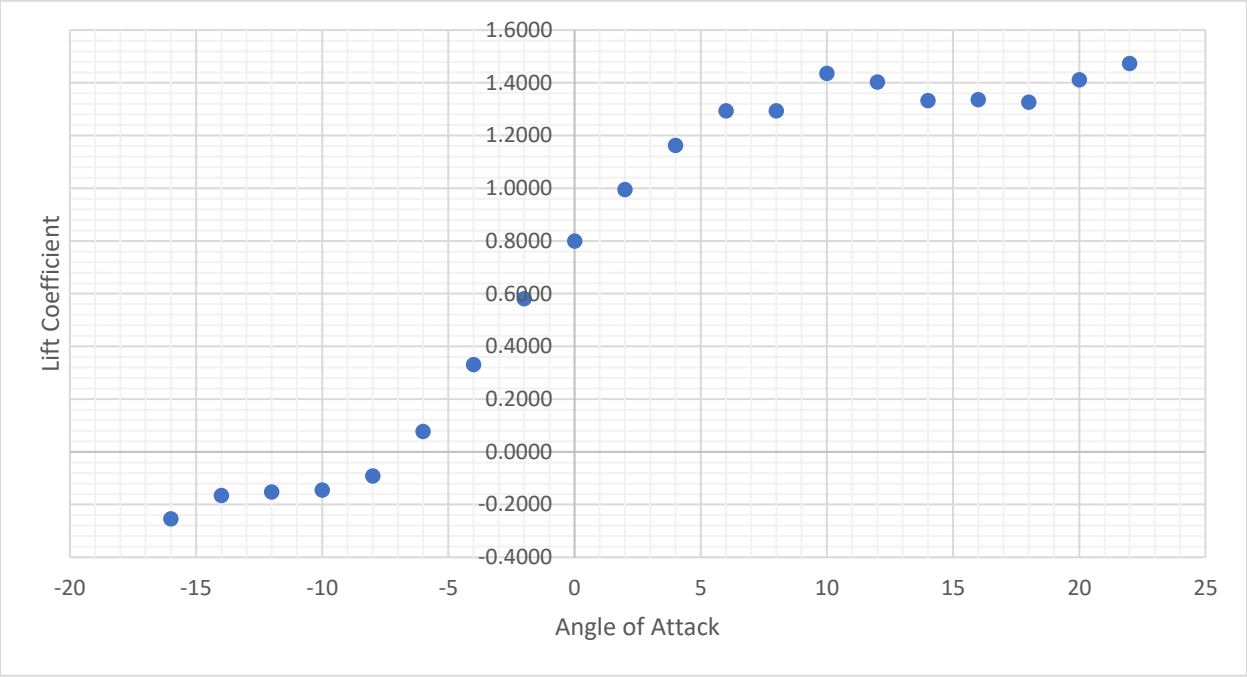

Figure 17: Lift coefficient as a function of angle of attack for 2D FX63-137 airfoil

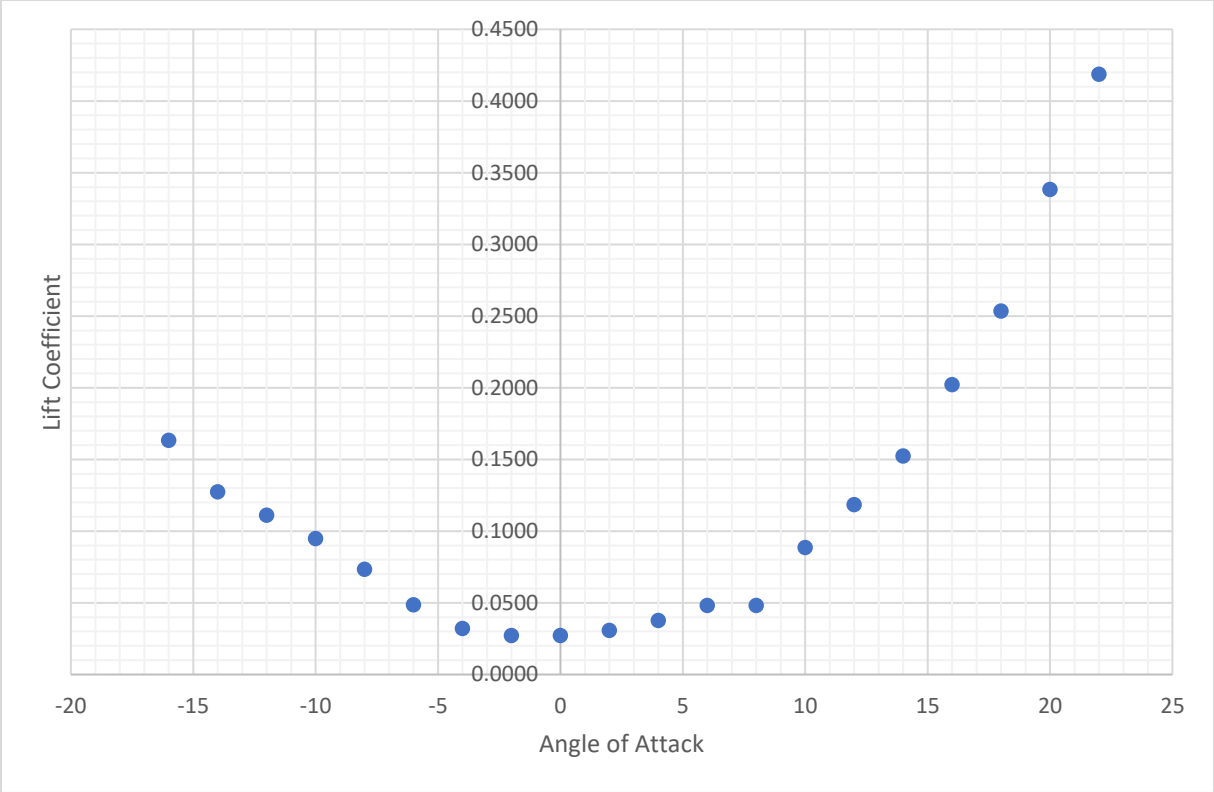

Figure 18: Drag coefficient as a function of angle of attack for 2D FX63-137 airfoil

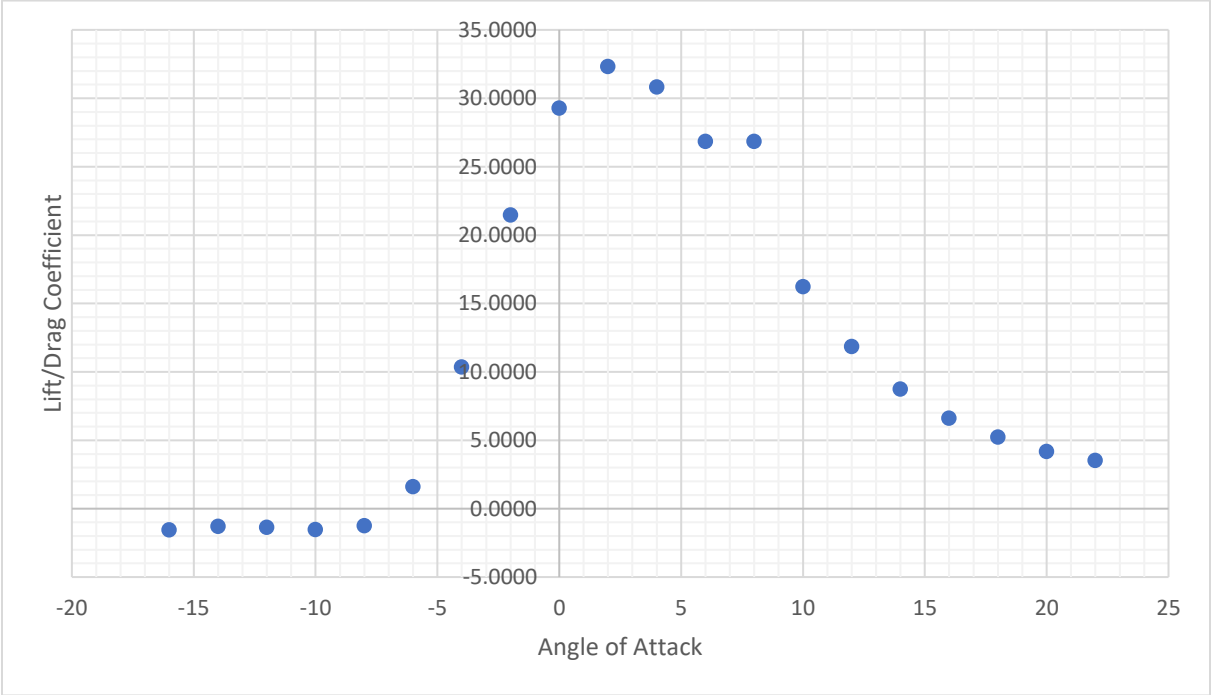

Figure 19: Lift/Drag coefficient as a function of angle of attack for 2D FX63-137 airfoil

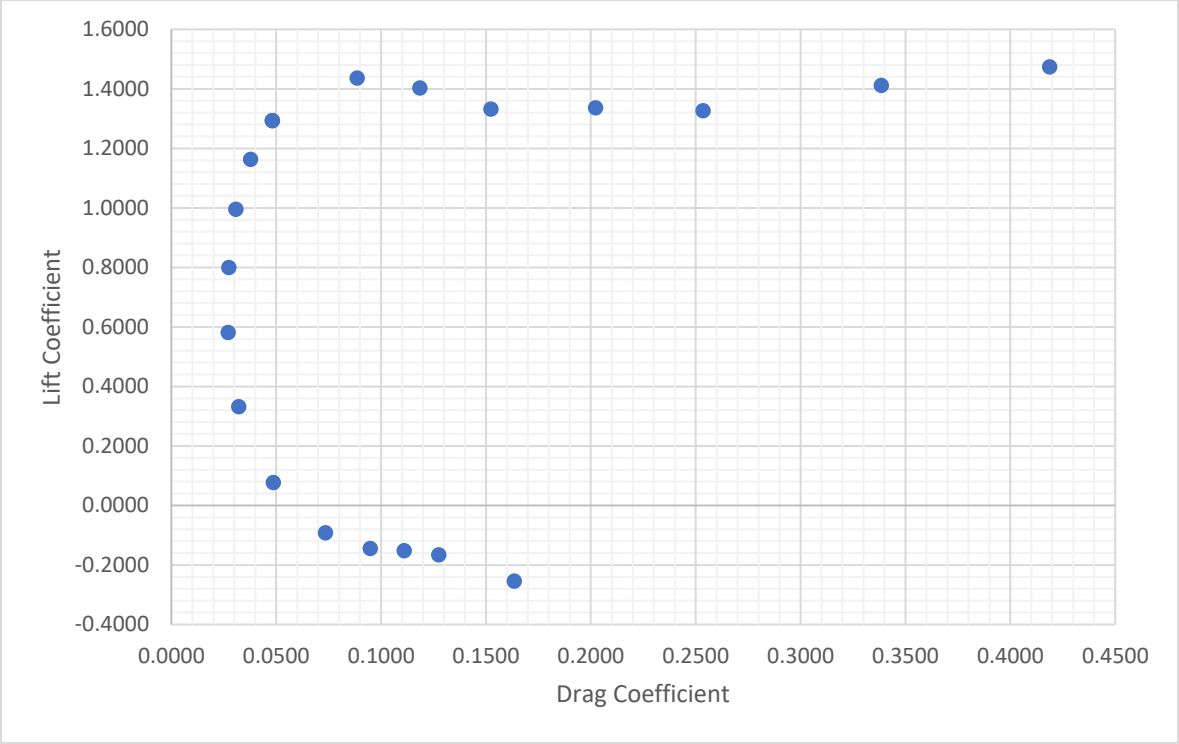

Figure 20: Lift coefficient as a function of drag coefficient for 2D FX63-137 airfoil

Note that the slope of the C_l curve for LRN-1015 in Figure 21 is mostly constant for small angles of attack too. This indicates that as angle of attack changes the lift coefficient changes linearly with a slope of 0.0883 . The slope of C_l curve starts to decrease significantly at an angle of attack of $\alpha = 12^{\circ}$. This is most likely due to flow separation. However, the lift coefficient starts to increase after the C_l value has gone over $\alpha = 18^{\circ}$. The stall angle can't be determined from the CFD experiment, but it was assumed to be $\alpha = 12^{\circ}$. The stall angle and lift slope are listed in Table 14 below. Lastly, the largest $\frac{C_l}{C_d}$ value is 25.30 and is obtained at an angle of attack of 4°. This can be observed in Figure 23 as well. This implies that the 4° AoA is the most optimal angle of attack as it generates the maximum lift at the list amount of drag.

Table 14: Stall angle, Lift slope and optimal angle of attack for LRN-1015 wing

Stall Angle $\boldsymbol{\alpha_{stall}}$ $[\boldsymbol{deg}]$	Lift Slope $[\frac{\boldsymbol{1}}{\boldsymbol{deg}}]$	Largest $\frac{\boldsymbol{C_l}}{\boldsymbol{C_d}}$	Largest $\frac{\boldsymbol{C_l}}{\boldsymbol{C_d}}$ angle $[\boldsymbol{deg}]$
12.0	0.0883	25.30	4.0

As was noted earlier, CFD was used to test two different airfoils. The first is the FX63-137 airfoil and the second is LRN-1015. The CFD results were used to find the airfoil that had the larger performance metric. The performance metric used in this design project consists of two parts. The first is the integral of $\frac{C_l}{C_d}$ from 0 to 20 degrees and is normalized by the wing volume. The second is the stall angle normalized by a factor. The three equations are shown below:

$$P_1 = \frac{1}{\forall}\int_0^{20} \frac{C_l}{C_d} d\alpha, \qquad P_2 = \frac{\alpha_{st}}{4} \qquad [1]$$

$$P_{total} = 0.6P_1 + 0.4P_2 \qquad [1]$$

To compute the integral numerically, the trapezoidal method was selected. The sample equations for this method are shown below.

$$\int_0^{20} \frac{C_l}{C_d} d\alpha = \sum_{i=1}^{12} \left(\frac{\left(\frac{C_l}{C_d}\right)_{i+1} + \left(\frac{C_l}{C_d}\right)_i}{2} \right) (\alpha_{i+1} - \alpha_i)$$

Since 2D CFD data was used to calculate the performance metrics, the value for the volume was assumed to be 1 m^3. The performance metrics for both airfoils are listed in Table 15.

Table 15: Performance metrics for FX63-137 and LRN-1015 calculated using 2D CFD data

Airfoil	P_1	P_2	P_{total}
FX63-137	372.13	3.5	225.03
LRN-1015	363.46	3	219.27

Since the FX63-137 has a higher performance metric, the 3D CFD simulation and the wind tunnel test will be performed for this airfoil only.

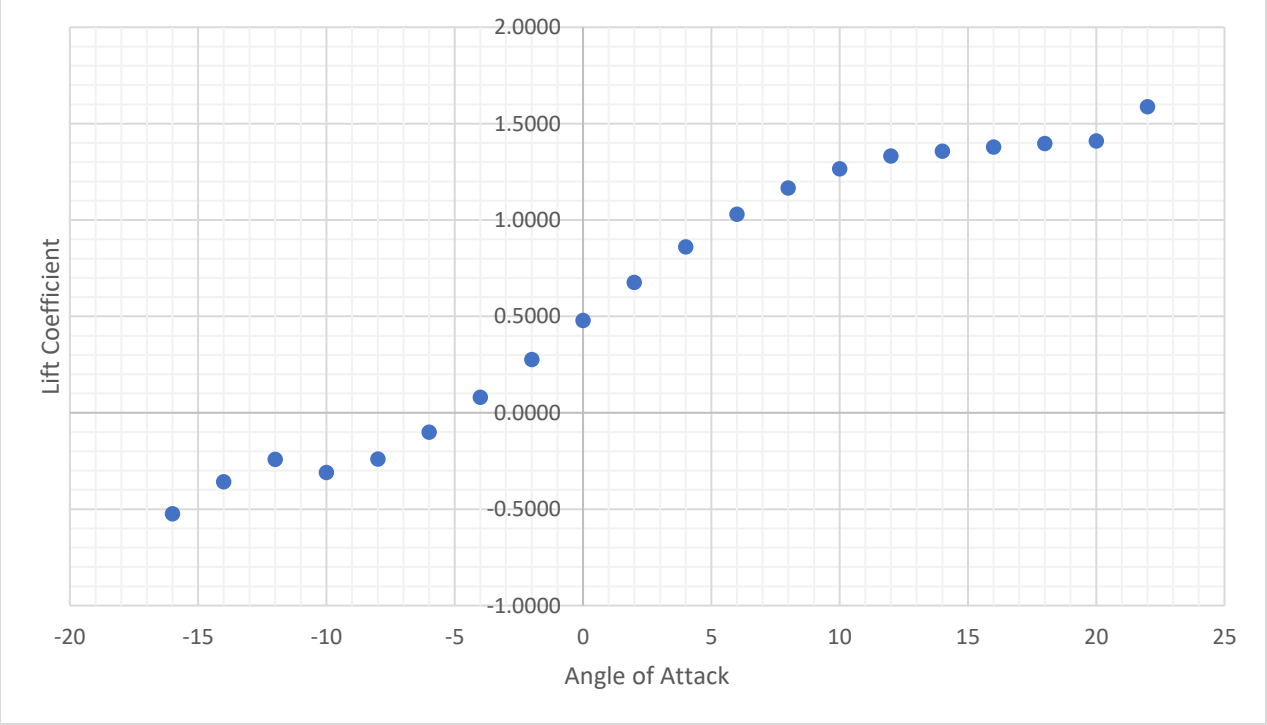

Figure 21: Lift coefficient as a function of angle of attack for 2D LRN-1015 airfoil

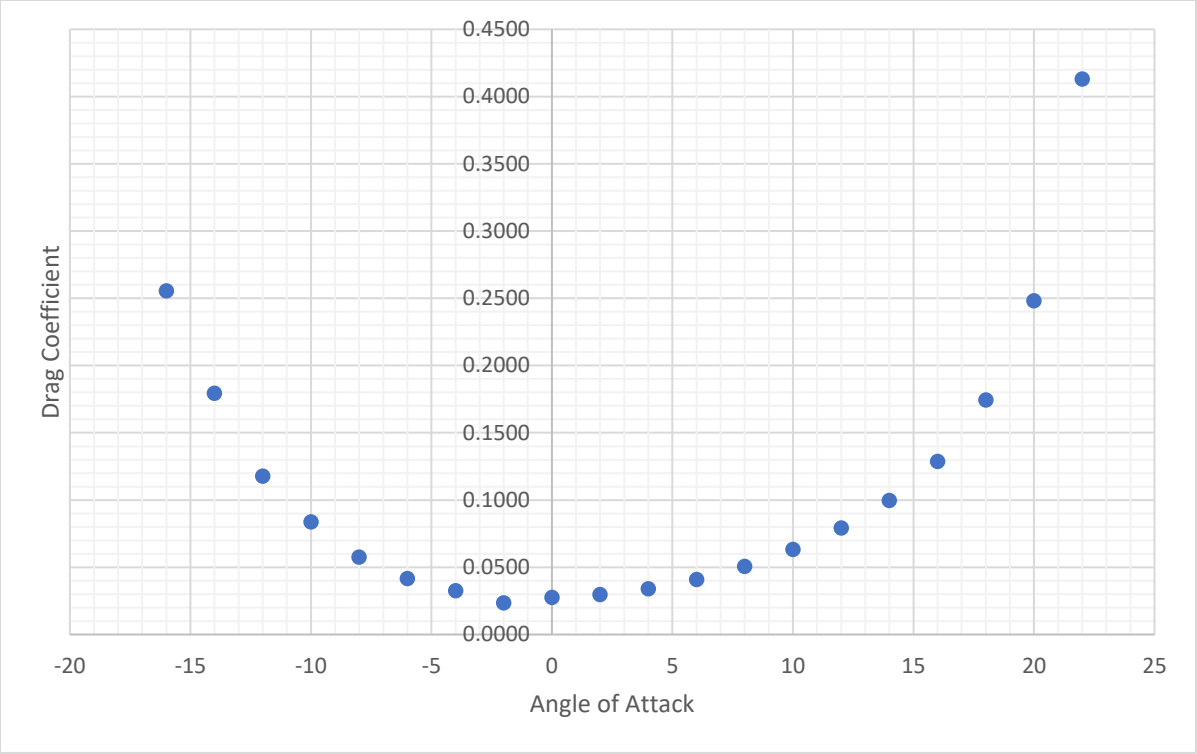

Figure 22: Drag coefficient as a function of angle of attack for 2D LRN-1015 airfoil

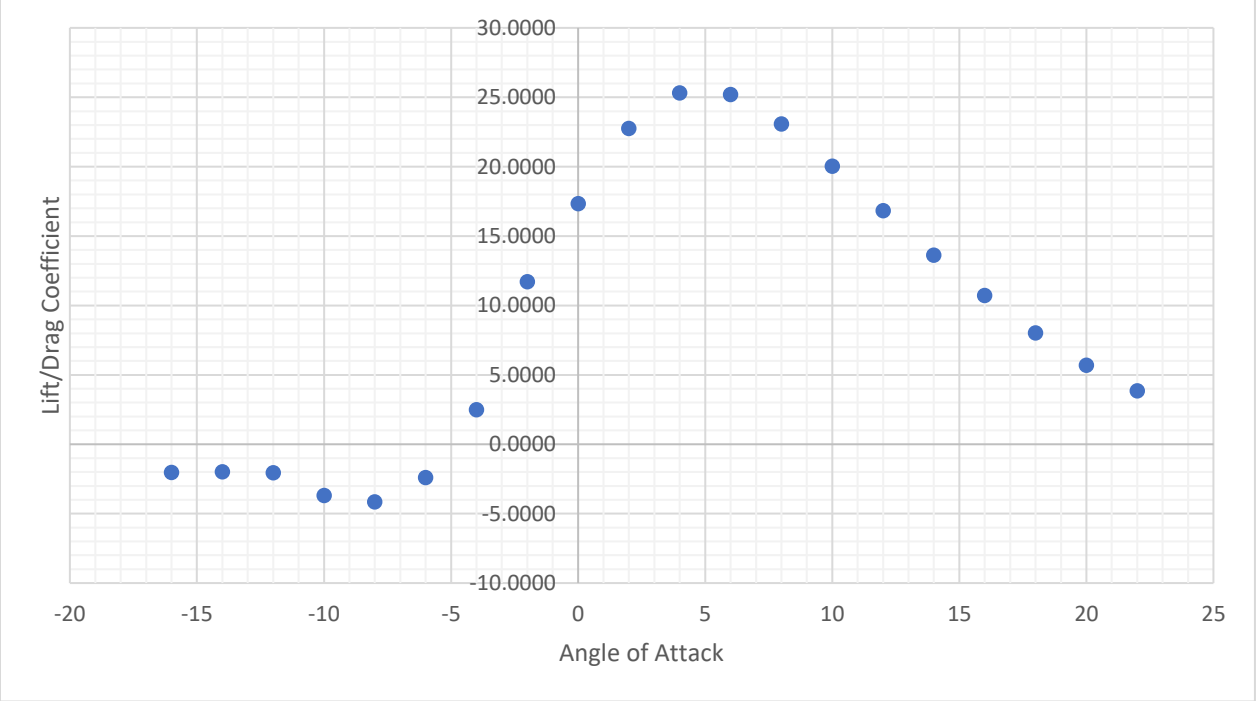

Figure 23: Lift/Drag coefficient as a function of angle of attack for 2D LRN-1015 airfoil

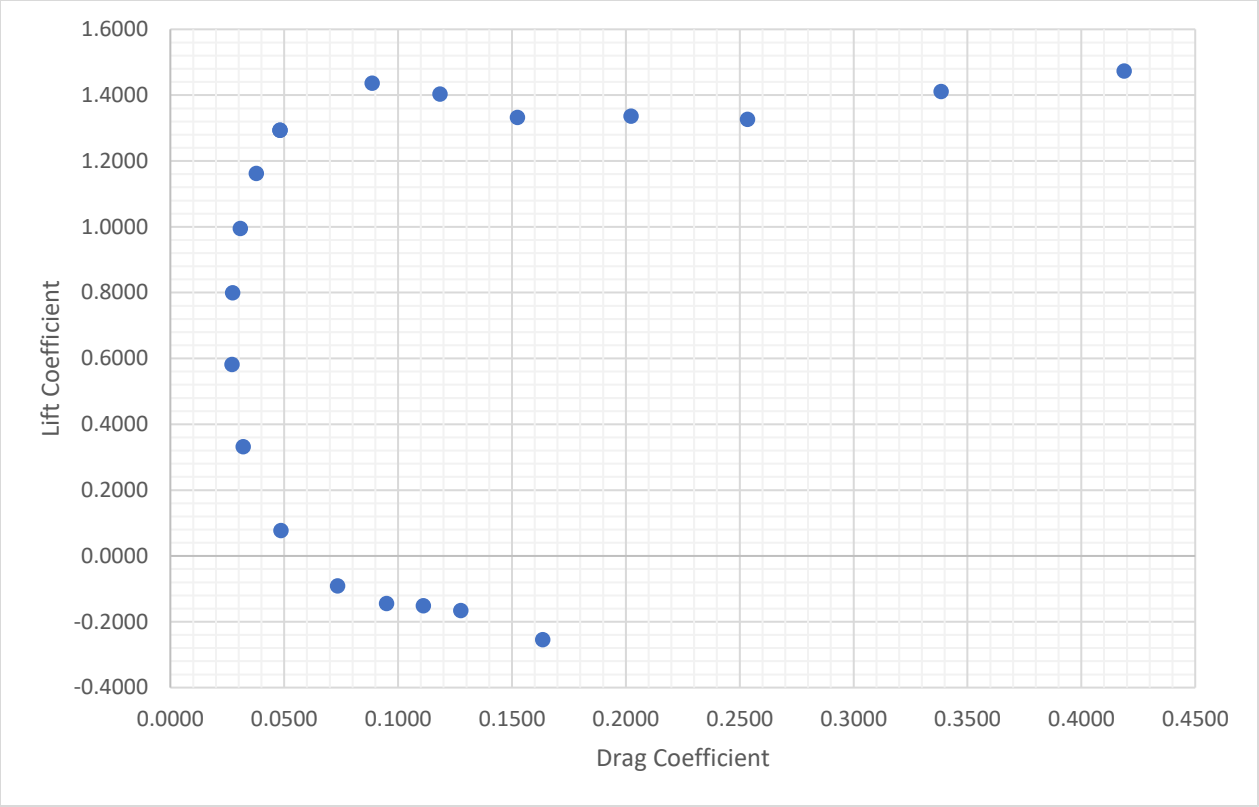

Figure 24: Lift coefficient as a function of drag coefficient for 2D LRN-1015 airfoil

Due to long computational time, a smaller subset of CFD simulations were performed for the 3D FX63-137 wing. The C_l slope for the 3D FX63-137, as seen in Figure 25, is constant for small angles of attack. This indicates that as angle of attack changes the lift coefficient changes linearly with a slope of 0.0188.

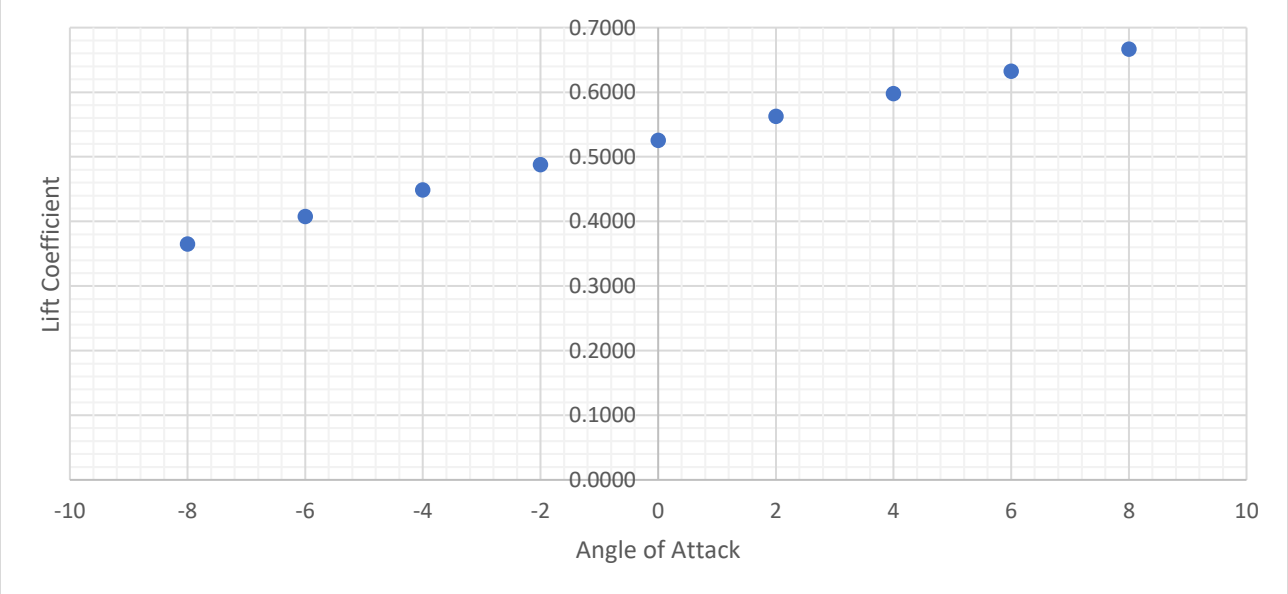

Figure 25: Lift coefficient as a function of angle of attack for 3D FX63-137 airfoil

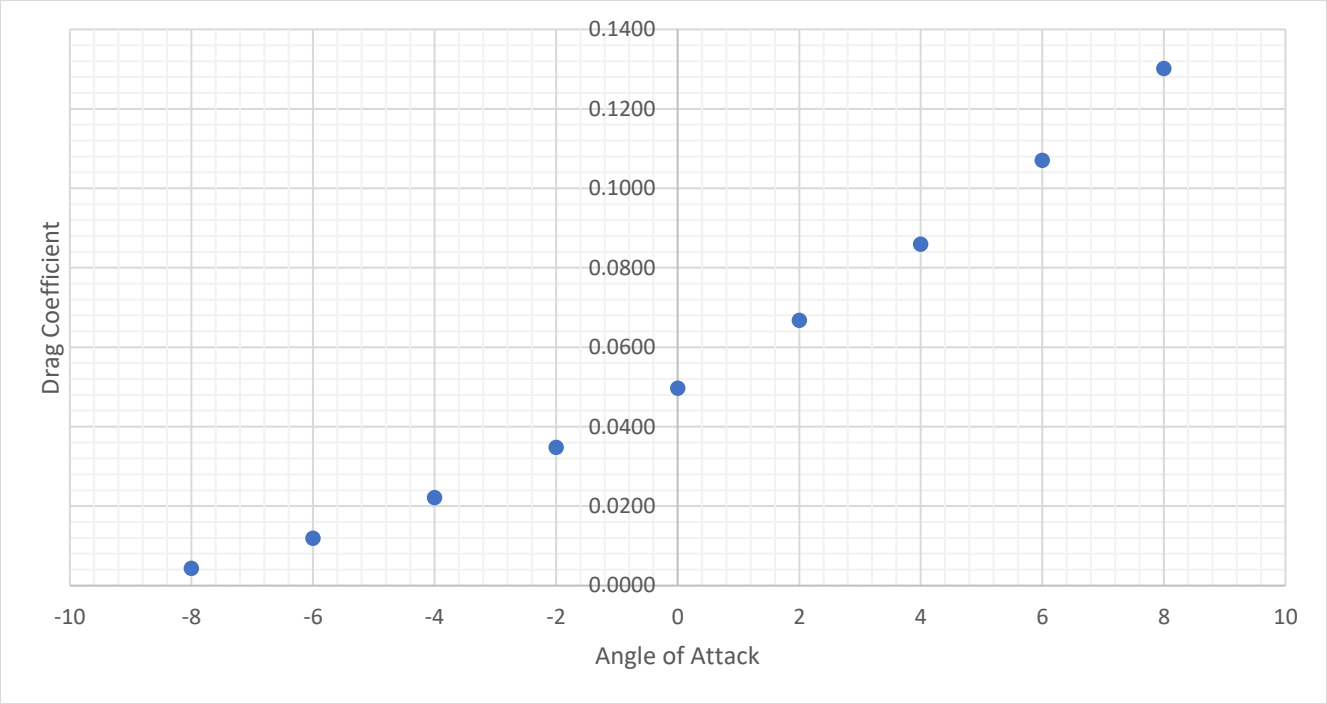

Figure 26: Drag coefficient as a function of angle of attack for 3D FX63-137 airfoil

Pressure Coefficient and Flow Visualisation

The Pressure coefficient is a dimensionless parameter that describes the relative pressure at a point in flow field. The pressure coefficient is calculated using the following equation:

$$C_p = \frac{P - P_\infty}{q_\infty}$$

If the pressure coefficient is negative this suggests that there is a low-pressure zone relative to the ambient pressure. If the pressure coefficient is positive this suggests that there is a high-pressure zone. Figure 27 is a plot of the pressure coefficient along the chord of the 2D FX63-137, which was obtained from CFD simulation at an angle of attack of $\alpha = 14^\circ$. Note that the differential pressure at the leading edge of the airfoil is the largest. This suggest that most of the lift being generated by the airfoil is produced close to the leading edge of the airfoil.

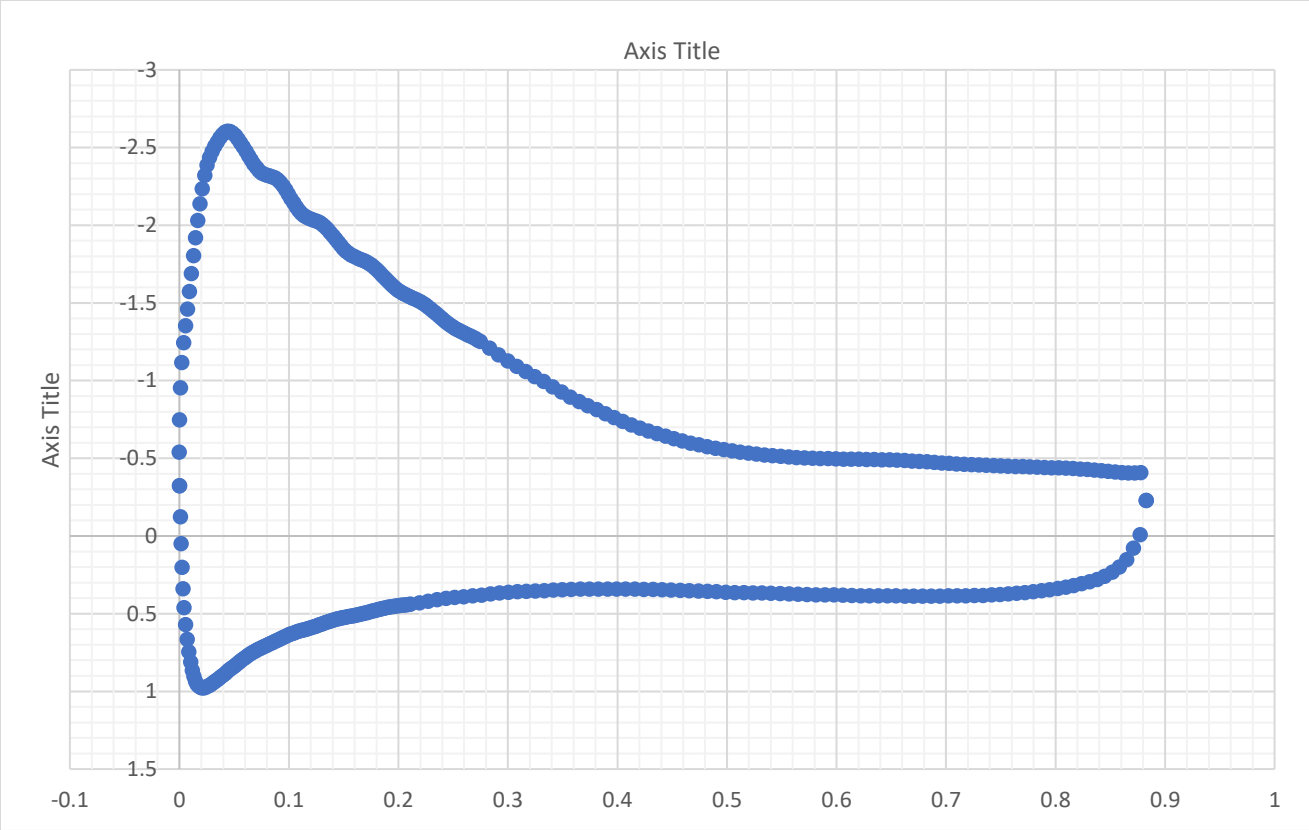

Figure 27: Pressure Coefficient as a function of chord length for the FX63-137

The pressure must fully recover so, the pressure coefficient at the top surface of the airfoil increases from a low value of -2.5 to a larger value of -0.5. However, the flow separates at around $c = 0.5$ from the leading edge of the airfoil with a pressure coefficient of approximately -0.5. The flow remains separated until approximately $c = 0.9$ from the leading edge where the pressure coefficient drops back to zero. Figure 28 shows the separated flow at an angle of attack of 14 degrees. The figure depicts streamlines of the flow and is colored by the velocity magnitude.

To keep the report concise the rest of the pressure coefficients, pressure contours, and streamline figures for FX63-137 are presented in the Appendix section.

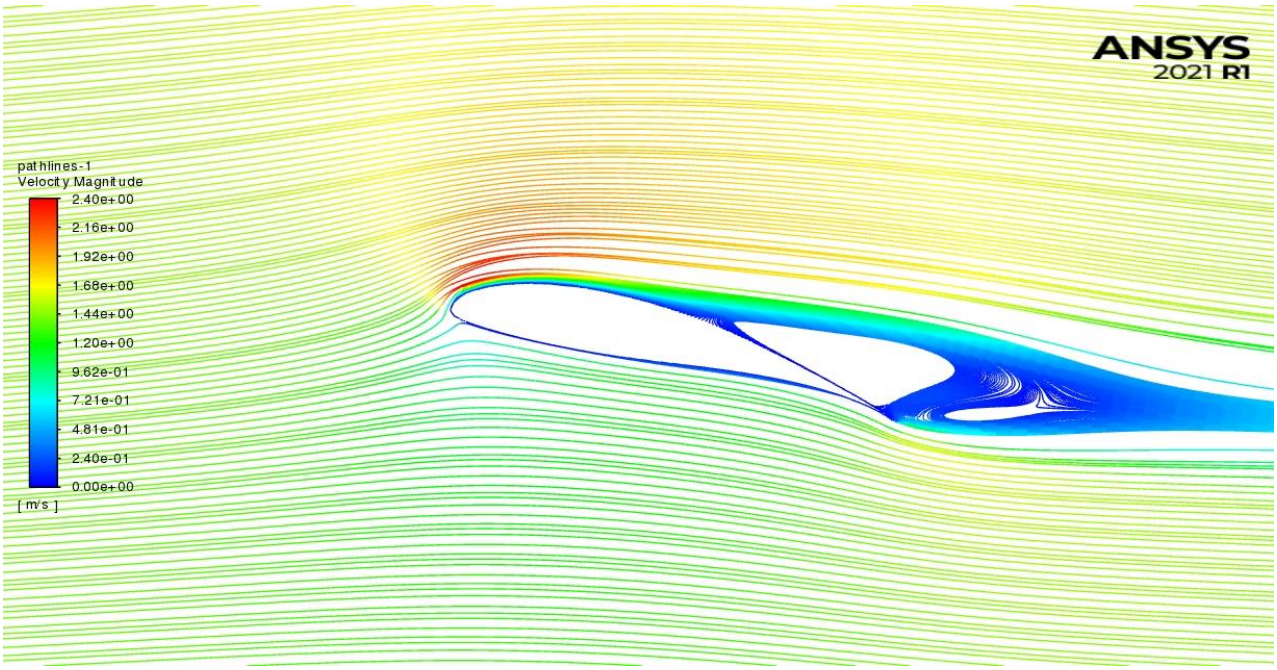

Figure 28: Streamlines used to visualize the flow at an angle of attack of 14 degrees.

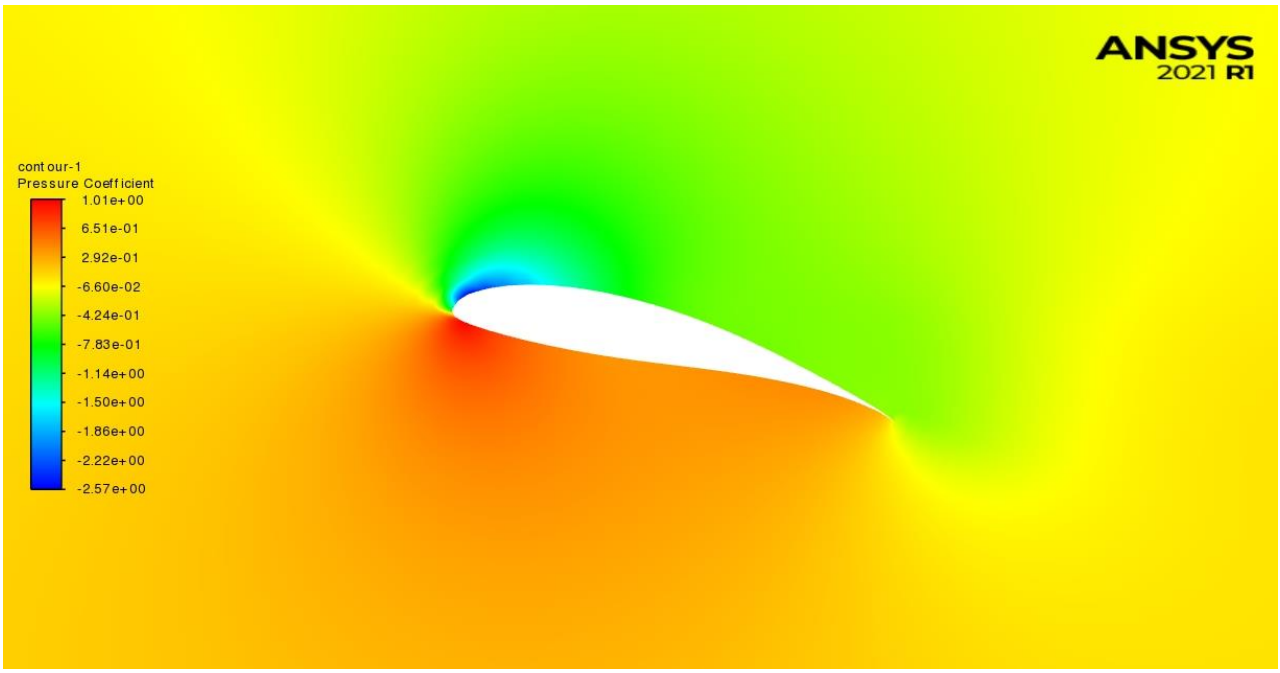

Figure 29: Pressure coefficient contours for the airfoil at an angle of attack of 14 degrees

Wind Tunnel Test

Calculation of Mean Forces

As was mentioned above the force data was sampled at a rate of 125 Hz for 20 seconds per angle of attack. To perform the analysis the mean value at each angle of attack had to be calculated. This was done by summing all the force data points for a specific angle of attack and dividing it by the total number of data points captured for the specific angle of attack. Most of the math shown here was carried out using MATLAB. However, this can be represented mathematically through the following equation:

$$Force_{mean} = \sum_{i=1}^{2500} F_{data\ point} = \frac{F_1 + F_2 + F_3 + \cdots + F_{2500}}{2500}$$

Note that the upper bound of the summation will be 2500 for each angle of attack. This is because data is being sampled at 125 Hz for 20 seconds.

$$N_{upper} = 20\ (sec) \times 125 \frac{data\ points}{sec} = 2500\ data\ points$$

Calculation of Aerodynamic Force Coefficients

It is normal practice in fluid mechanics to report metrics in nondimensional terms. This makes it easier to scale the data obtained for different situations. In this case the lift and drag will be converted to their equivalent nondimensional coefficients by dividing the force magnitudes by a reference area and the dynamic pressure. This is represented mathematically below:

$C_L = \frac{L}{qA_{ref}}$ and $C_D = \frac{D}{qA_{ref}}$

where, C_L is the lift coefficient, L is the lift force $[N]$, D is the drag force $[N]$, $q = \frac{1}{2}\rho V_\infty^2$ is the freestream dynamic pressure $[Pa]$, and $A_{ref}$is a reference area.

The reference area is usually calculated by multiplying the wingspan by the chord length. Since the wing tested has an elliptical planform area the area is calculated using SOLIDWORKS. Table 16 lists important geometric parameters of each wing.

Table 16: Important geometric parameters of FX63-137

Wing Model	Span S, $[\boldsymbol{m}]$	Chord C, $[\boldsymbol{m}]$	Reference Area $\boldsymbol{A_{ref}}$, $[\boldsymbol{m^2}]$	Wing Volume $\forall$ $[\boldsymbol{m^3}]$
Rectangular	0.260	0.08100	0.02106	1.4248×10^{-4}
Elliptical	0.257	0.081 to 0.01230	0.01655	9.51×10^{-5}

Sample calculation for calculating reference area is shown below:

$$A_{ref} = Span \times Chord$$

$$A_{ref} = 0.260\ m \times 0.08100\ m = \ 0.02106\ m^2$$

Sample calculation for calculating the freestream dynamic pressure is shown below:

$$q = \frac{1}{2}\rho V_\infty^2$$

$$q = \frac{1}{2}(1.0563\frac{kg}{m^3})(18.2\frac{m}{s})^2$$

$$q = 174.94\ [Pa]$$

Sample calculation for calculating lift and drag coefficients are shown below:

$$C_L = \frac{L}{qA_{ref}}$$

$$C_L = \frac{1.7673\ N}{(174.94\ Pa)(0.01655\ m^2)}$$

$$C_L = \ 0.6086$$

Note all the lift and drag coefficients have been calculated using MATLAB and are listed in table 17. Unfortunately, due to some design problems the rectangular wing profile wasn't tested. Therefore, the wind tunnel experiment was only conducted on the elliptical FX63-137 wing.

Table 17: Lift and drag coefficients obtained for the elliptical FX63-137 wing

Angle of Attack, $\boldsymbol{\alpha}\ [\boldsymbol{deg}]$	Lift Coefficient, $\boldsymbol{C_l}$	Drag Coefficient, $\boldsymbol{C_d}$	Lift/Drag Coeff, $\frac{\boldsymbol{C_l}}{\boldsymbol{C_d}}$
0	0.6104	0.0453	13.4702
-2	0.4902	0.0427	11.4819
-4	0.3501	0.0416	8.4086
-6	0.2312	0.0453	5.1005
-8	0.1115	0.0573	1.9471
-10	-0.0048	0.0810	-0.0587
-12	-0.0827	0.1103	-0.7490
-14	-0.1291	0.1346	-0.9593
-16	-0.0952	0.1516	-0.6280
0	0.6065	0.0367	16.5027
2	0.7169	0.0419	17.0944
4	0.8259	0.0493	16.7483
6	0.9358	0.0586	15.9747
8	1.0241	0.0680	15.0716
10	1.1295	0.0810	13.9430
12	1.2092	0.0980	12.3402
14	1.2649	0.1165	10.8598
16	1.2837	0.1374	9.3462
0	0.5381	0.0208	25.8703

The experimental lift and drag coefficients for the elliptical FX63-137 wing are plotted on figures Figure 30 and Figure 31 respectively. As one can see at an angle of attack of zero the FX63-137 wing is creating a lift coefficient of approximately $C_L = 0.5850$. This is due to the asymmetric shape of the FX63-137 wing profile. Moreover, at this angle of attack the FX63-137 wing generates approximately a drag coefficient of $C_D = 0.03427$. Note that the slope of the C_L curve is mostly constant for small angles of attack. This indicates that as angle of attack changes the lift coefficient changes linearly with a slope of 0.0619 . The slope of C_L curve starts to decrease significantly at an angle of attack of $\alpha = 16^{\circ}$. This is most likely due to flow separation. At this stage the boundary layer separates from the surface of the airfoil. This causes the lift to drop significantly and the drag to increase. For the FX63-137 the C_L slope starts to decrease at an angle of attack of $\alpha = 16^{\circ}$. The stall angle and lift slope are listed in table 18 below. Lastly, the largest $\frac{C_L}{C_D}$ value is 17.09 and it obtained at an angle of attack of 2 degrees. This can be observed on Figure 30 as well. This implies that the 2-degree AoA is the most optimal angle of attack as it generates the maximum lift at the list amount of drag.

Table 18: Stall angle, Lift slope and optimal angle of attack for FX63-137 wing

Stall Angle $\boldsymbol{\alpha_{stall}}$ $[\boldsymbol{deg}]$	Lift Slope $[\frac{\mathbf{1}}{\boldsymbol{deg}}]$	Largest $\frac{\boldsymbol{C_L}}{\boldsymbol{C_D}}$	Largest $\frac{\boldsymbol{C_L}}{\boldsymbol{C_D}}$ angle $[\boldsymbol{deg}]$
16.0	0.0619	17.09	2.0

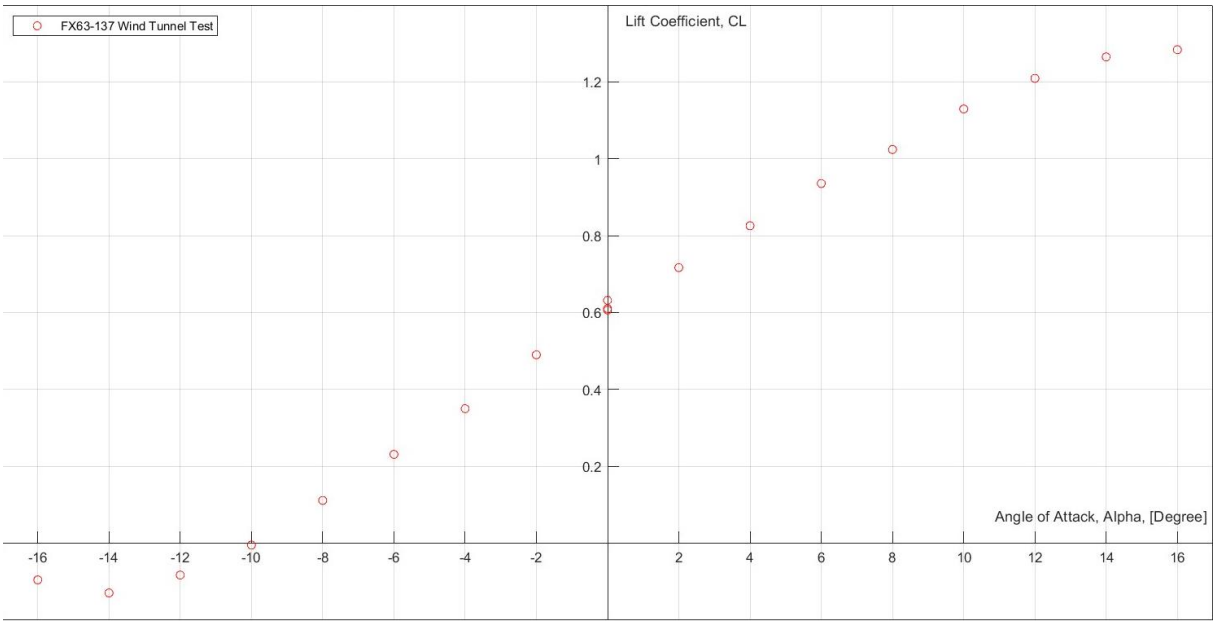

Figure 30: Lift coefficient as a function of angle of attack for FX63-137 elliptical wing

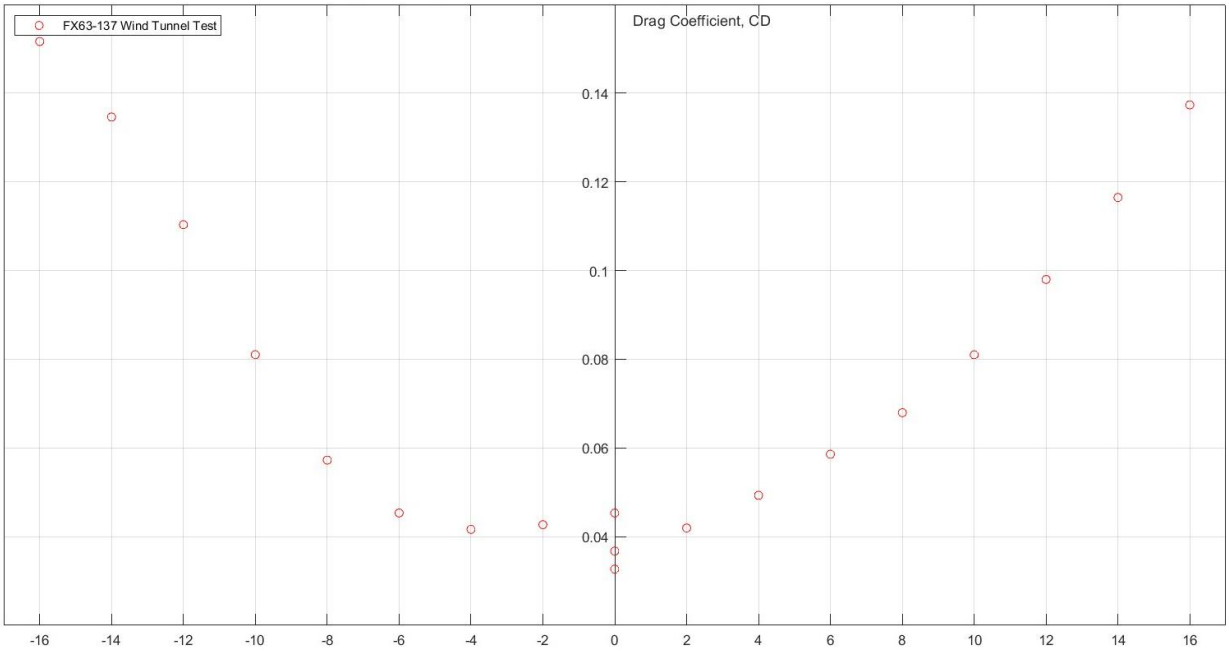

Figure 31: Drag coefficient as a function of angle of attack for FX63-137 elliptical wing

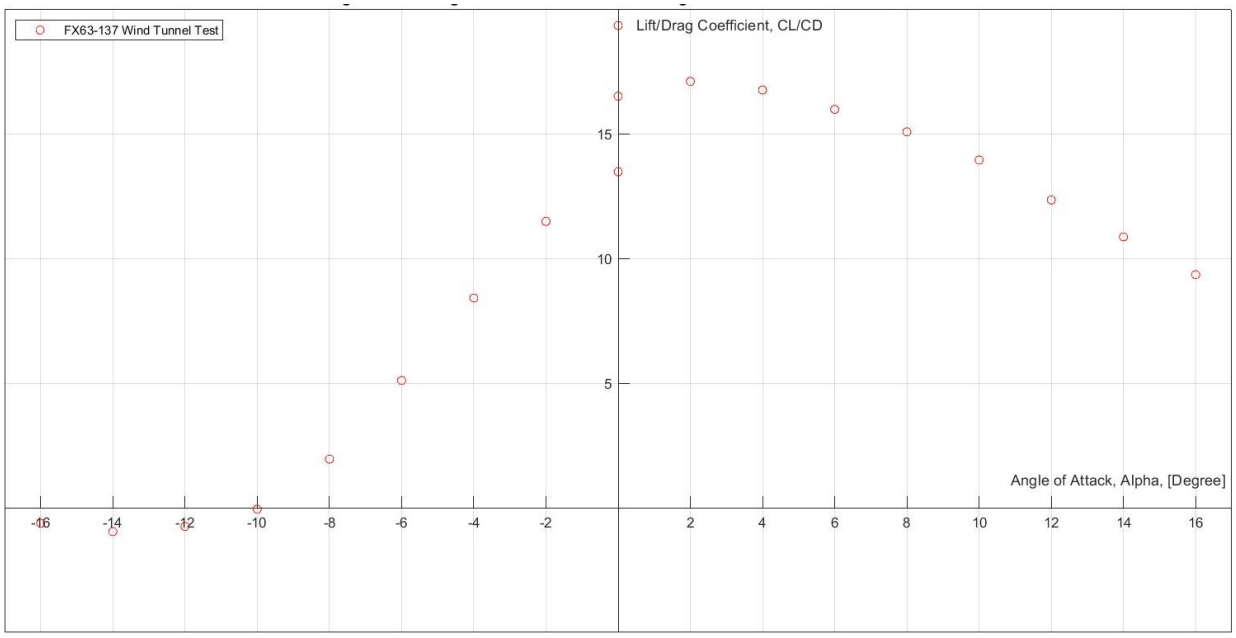

Figure 32: Lift/Drag coefficient as a function of angle of attack for FX63-137 elliptical wing

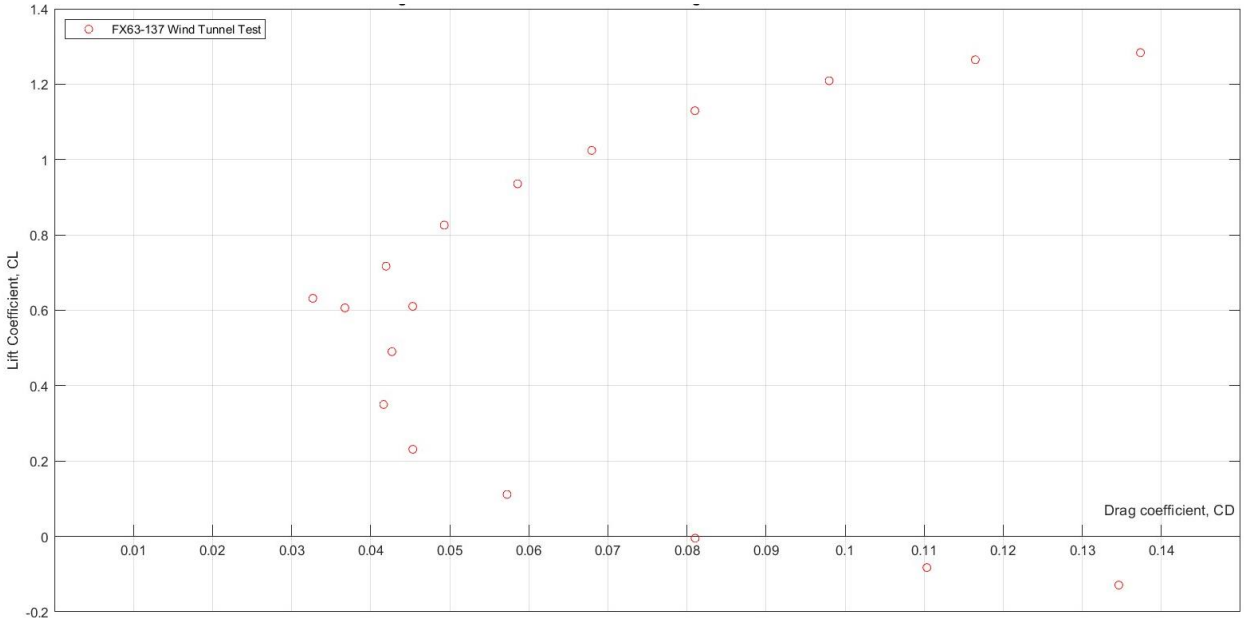

Figure 33: Lift coefficient as a function of drag coefficient for FX63-137 elliptical wing

Validation and Comparison of Results

To compare our experimental results with the literature values the experimental Reynold's number must be calculated first. To calculate the Reynold's number the following equation is used:

$$Re = \frac{\rho C V_\infty}{\mu}$$

Where C is the chord length of the airfoil. Plugging values from table 11 and 16 we get:

$$Re = \frac{1.0563\ \left(\frac{kg}{m^3}\right) 0.08100(m) 18.2(\frac{m}{s})}{1.805\ \times 10^{-5}(\frac{kg}{ms})}$$

$$Re = 86271.33$$

The literature data at $Re = 102100$ was obtained from reference [3] for the FX63-137(B) airfoil. The literature data was then plotted in MATLAB against the experimental and CFD results. Figure 38 and Figure 39 are the plots of lift and drag coefficient, respectively, comparing the experimental and the literature data.

Comparing the 2D CFD results and Experimental Results

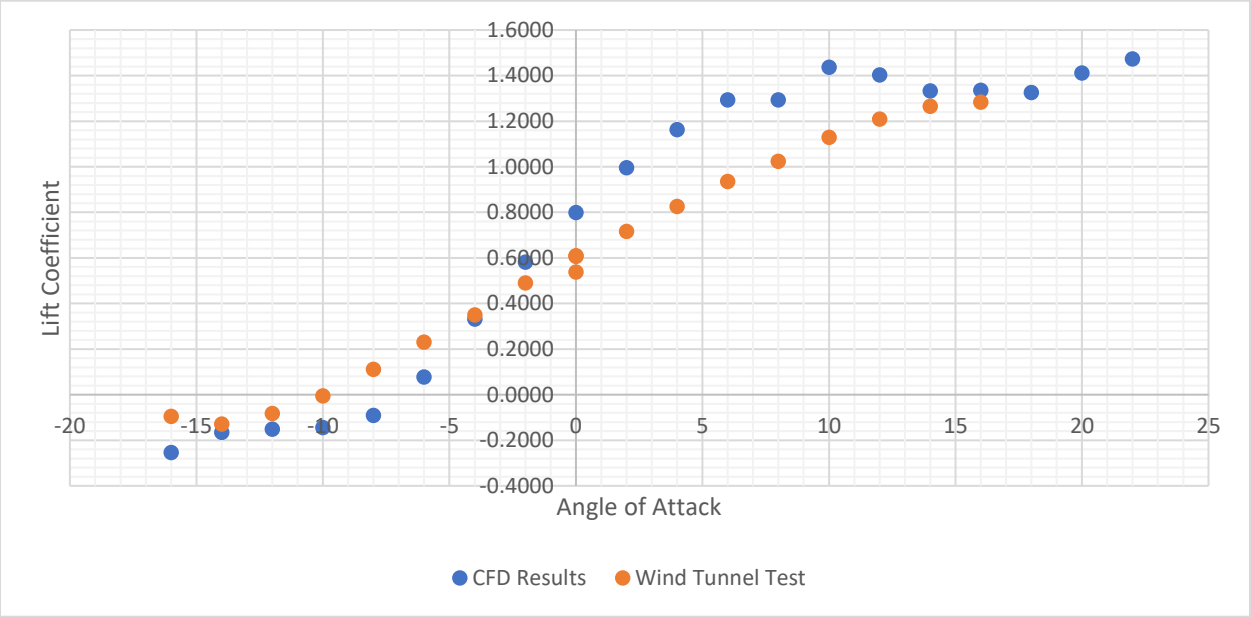

Figure 34: Lift coefficient as function of angle of attack for FX63-137 airfoil

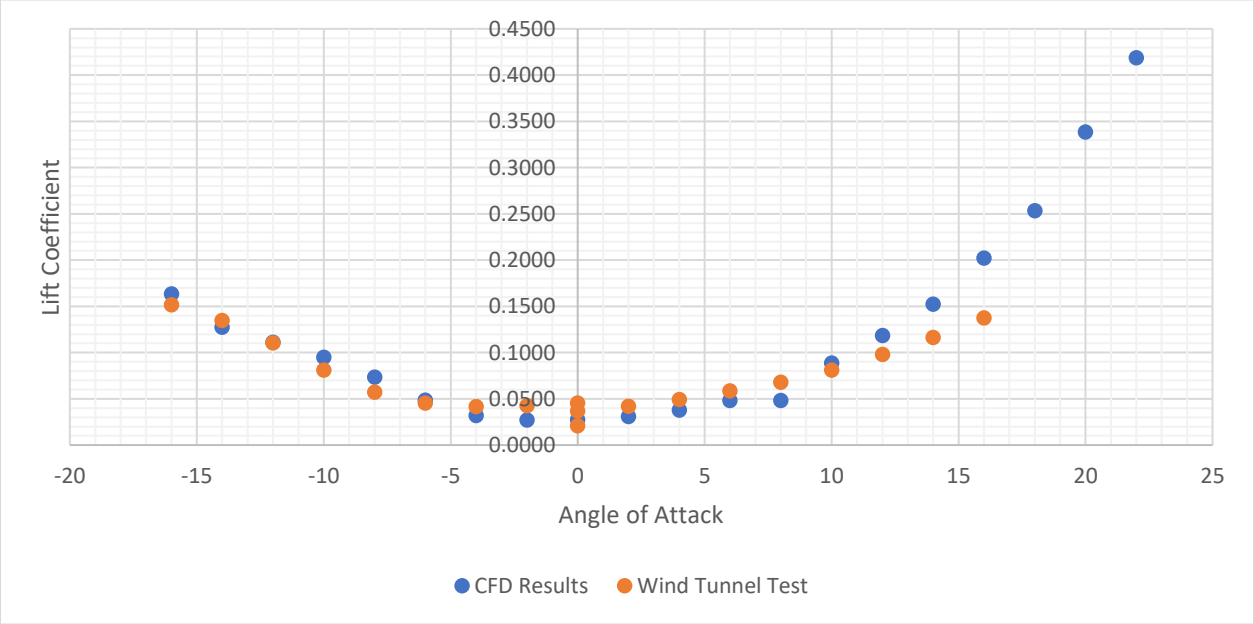

Figure 35: Drag coefficient as a function of angle of attack for FX63-137

From Figures Figure 34 and Figure 35 the shapes of the experimental lift and drag coefficient curves follow that of the CFD curves. However, the experimental lift values obtained have a smaller lift slope than the ones from 2D CFD simulations. This is expected as 3D wings experience downwash which influences the geometric angle of attack while the 2D CFD simulations do not experience downwash. The experimental lift curve paces through $C_L = 0.5850$ at an angle attack of 0 while the CFD curve has a $C_l = 0.7995$ at the 0 angle of attack. The experimental drag coefficient values match very well to values obtained from CFD simulations.

Comparing the 3D CFD results and Experimental Results

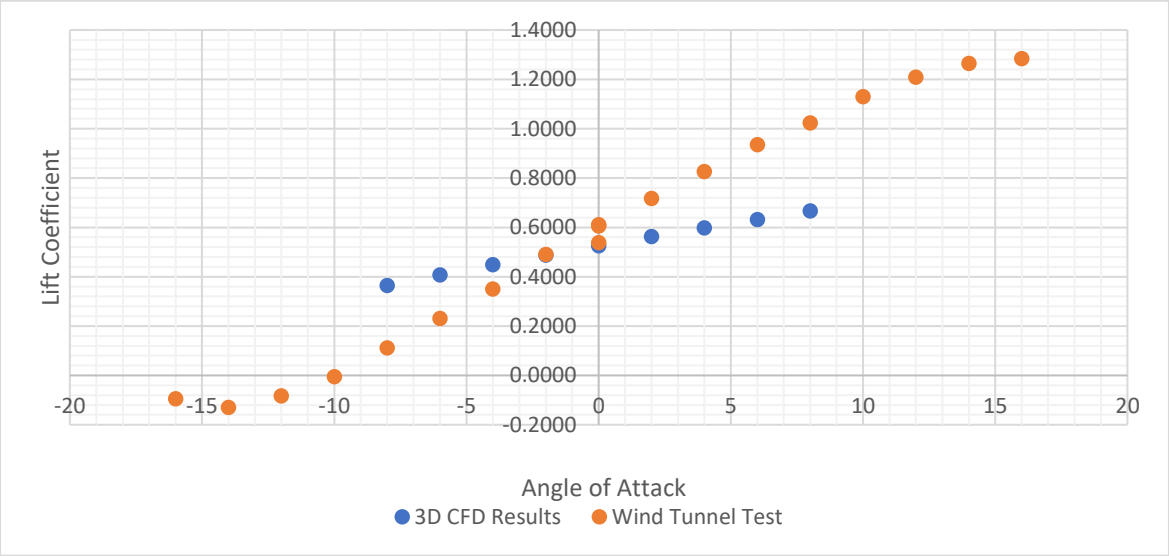

Figure 36: Lift coefficient as function of angle of attack for FX63-137 airfoil

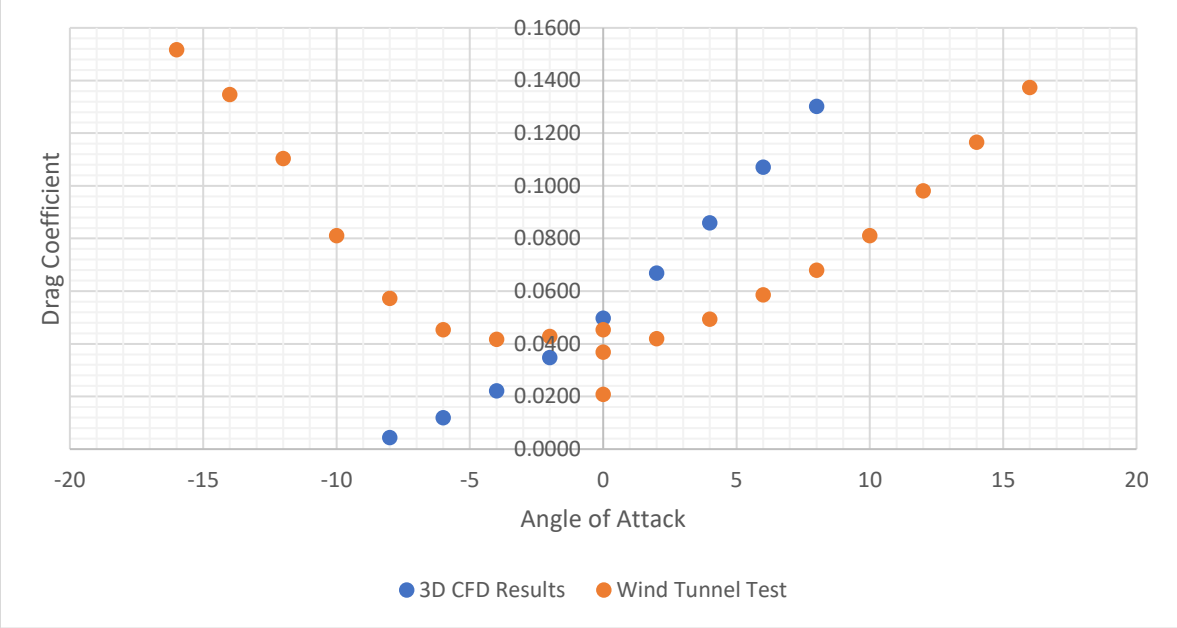

Figure 37: Drag coefficient as function of angle of attack for FX63-137 airfoil

The shapes of the experimental lift and drag coefficient curves follow that of the 3D CFD curves. However, the experimental lift values obtained have a larger lift slope than the ones obtained from 3D CFD simulations. Note that due to computational limitations the 3D CFDs were run at lower-than-normal mesh resolutions. Therefore, the data obtained from them is most likely erroneous. The experimental lift curve paces through $C_L = 0.5850$ at an angle attack of 0 which matches that of the 3D CFD curve which is $C_l = 0.5257$. These two values match because the 3D CFD models the downwash behavior too. The experimental drag coefficient does not match very well to values obtained from 3D CFD simulations.

Comparing the Experimental and Literature Values

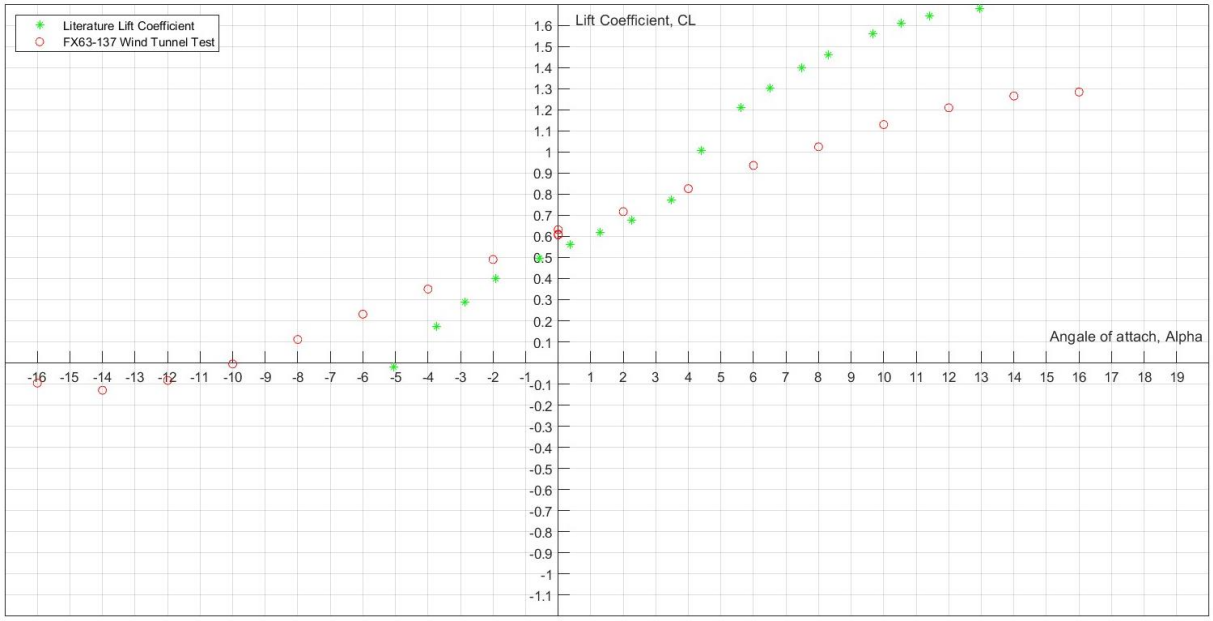

Figure 38: Lift coefficient as function of angle of attack for FX63-137 airfoil [3]

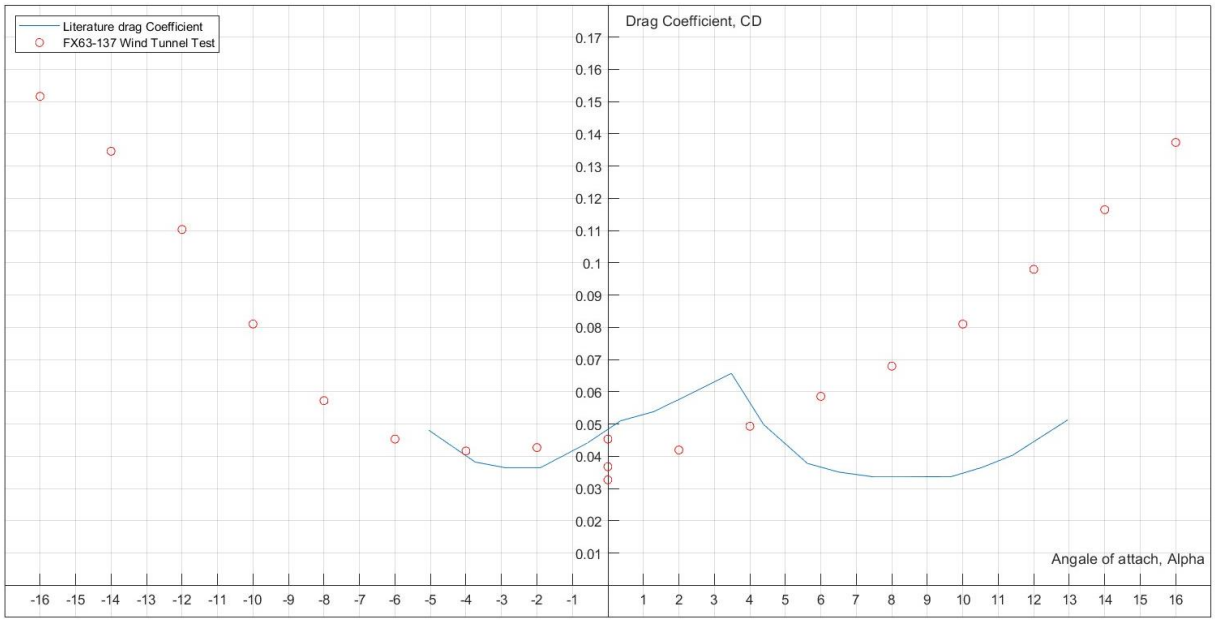

Figure 39: Drag coefficient as function of angle of attack for FX63-137 airfoil [3]

The shapes of the experimental lift and drag coefficient curves follow that of the literature curves. However, the experimental lift values obtained have a smaller lift slope than the literature values. This is most likely due to wind tunnel errors such as solid and wake blockage effects. The experimental lift curve paces through $C_L = 0.5850$ at an angle attack of 0° while literature curve has a $C_l = 0.5285$. The experimental drag coefficient values do not match well to values obtained from literature. The FX63-137 airfoil was 3D printed and its surface was taped with Tuck Tape to reduce surface friction. However, there were ridges on the tape that would create

more drag. Finally, there were vibrations at larger angles of attack. This was due to the tolerance between the connecting pins and the mounting rod.

Comparing the Experimental and Panel Method Results

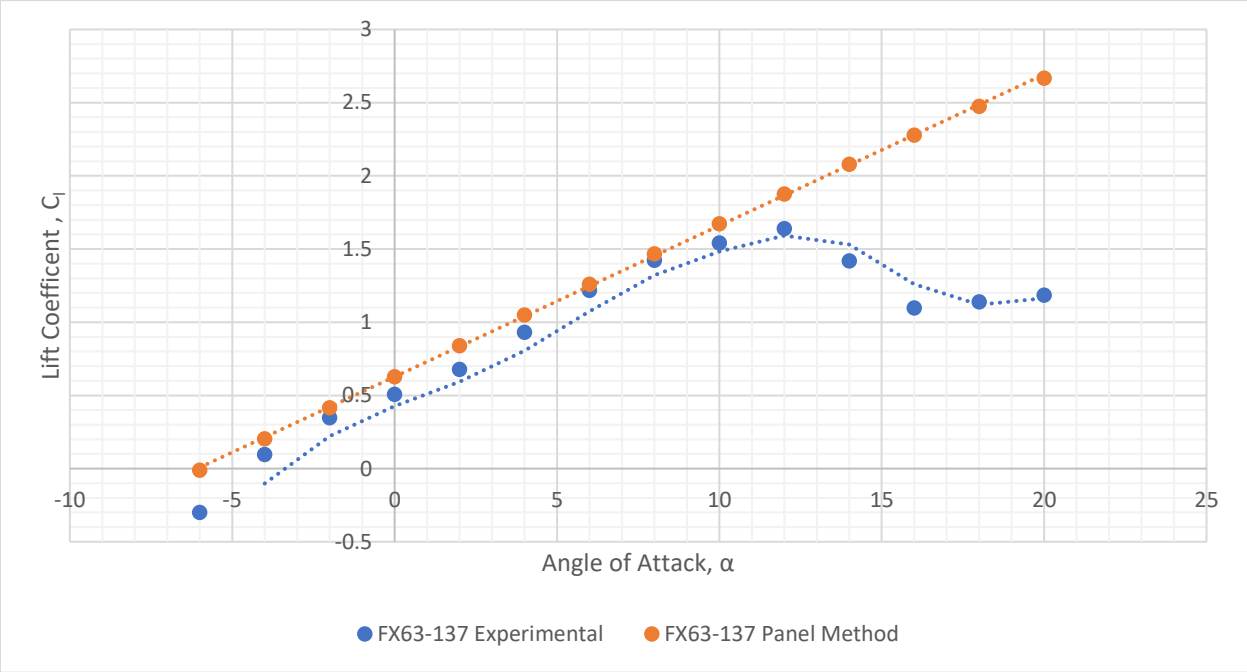

Figure 40: Experimental and panel method results of lift coefficient as function of angle of attack for FX63-137 airfoil

Figure 40 is the plot of experimental and panel method approximation of lift coefficient as a function of angle of attack for FX 63-137. The panel method results for FX 63-137 agree closely with the experimental results at low angles of attack. At low angles of attack (approximately between – 5 to 10 degrees) the slope of the experimental data is 0.1034 while the slope of the panel method approximation is 0.1033. The panel method cannot predict the stall behavior and the predicted values above 10° are incorrect. This is because the panel method relies on inviscid flow models while stall is a viscous phenomenon. Table 18 lists some useful information used during the panel method approximation. The panel method code was highly sensitive to number of panels used. Through trial and error 190 panels were selected as it provided the best results. Furthermore, the last panel was left unsolved so that the Kutta-Joukowski condition could be implemented on the last panel instead.

Table 19: Values used during the panel method lift coefficient prediction of the FX 63-137

Freestream Velocity, $\boldsymbol{V_\infty}[\frac{\boldsymbol{m}}{\boldsymbol{s}}]$	Density, $\boldsymbol{\rho}[\frac{\boldsymbol{kg}}{\boldsymbol{m^3}}]$	Number of Panels, **N**	Reynolds Number, **Re**
1.47	1.225	190	100,000

Conclusion

The aerodynamic characteristics of two airfoils (namely FX63-137 and LRN-1015) were tested in subsonic flow regimes at a Reynolds number of approximately $Re = 100000$. Different methods were used to test the airfoils. First, the flow behavior around the two airfoils were modeled using 2D CFD simulations. The airfoil's performance metrics were then calculated and compared to one another. It was determined that the FX63-137 has the larger performance metric. The performance metrics for the airfoils were calculated to be $P_{FX63-137} = 225.03$ and $P_{LRN-1015} = 219.27$. Next, 3D CFD simulations were performed for the FX63-137 wing. The results are discussed in the discussion section but due to computational limitations the 3D CFD results were not accurate. Finally, an elliptical wing model of the FX63-137 with a planform area of $0.01655\ m^2$ and wing volume of $9.51 \times 10^{-5} m^3$ was created and tested in a wind tunnel. The aerodynamic force data were collected using a 6-axis force transducer mounted beneath the airfoils. After the data was treated the lift and drag coefficients were calculated. The lift coefficient results obtained from the 2D CFD were larger than those obtained through wind tunnel tests. The lift results obtained from the wind tunnel test were lower than those obtained through literature. In conclusion, the FX63-137 was selected as an optimal wing for a UAV traveling at 18.2 m/s for the following reasons. The FX63-137 has a large stall angle of 16 degrees when compared to the LRN-1015. Moreover, this airfoil profile has a larger lift slope when compared to the LRN-1015. Lastly, this airfoils max $\frac{C_l}{C_d}$ is 32.33 which occurs at an angle of attack of 2 degrees while the LRN-1015 has a $\frac{C_l}{C_d}$ of 25.30 which occurs at 4 degrees.

References

1. *ENME 570/670: Aerodynamics Project: Wing Design*, University of Calgary, Calgary, Alberta, Canada, Oct. 2022. Accessed: Nov. 2, 2022. [Online] Available: https://d2l.ucalgary.ca/d2l/le/content/470932/viewContent/5543979/View
2. *Lift and Drag for Symmetric and Cambered Airfoils*, University of Calgary, Calgary, Alberta, Canada, Oct. 2022. Accessed: Oct. 14, 2022. [Online] Available: https://d2l.ucalgary.ca/d2l/le/content/470932/viewContent/5538333/View
3. M. S. Selig and B. D. McGranahan, "Wind Tunnel Aerodynamic Tests of Six Airfoils for Use on Small Wind Turbines", *Journal of Solar Energy Engineering*, vol. 126, Jan. 2004.
4. R. M. Hicks, S. E. Cliff, "An Evaluation of Three Two-Dimensional Computational Fluid Dynamics Codes Including Low Reynolds Numbers and Transonic Mach Numbers", National Aeronautics and Space Administration, Moffett Field, California, USA, 102840, Jan. 1991, Accessed: Nov. 14, 2022. [Online]. Available: https://ntrs.nasa.gov/api/citations/19910007688/downloads/19910007688.pdf

Appendix (Flow Visualization and C_p)

C_p contour at -16 degrees

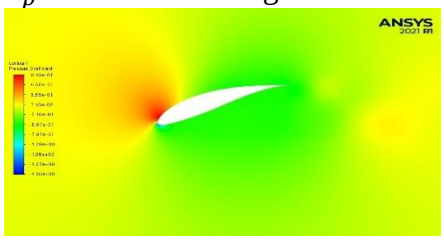

Streamline at -16 degrees

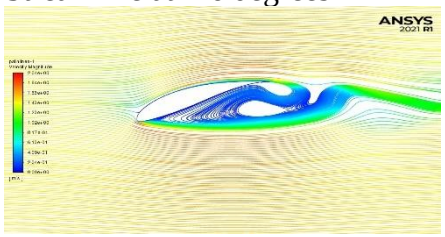

C_p contour at -14 degrees

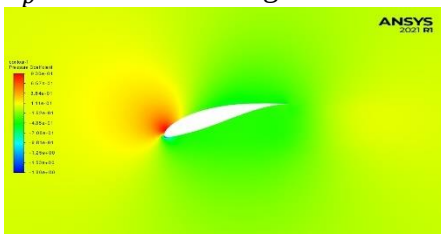

Streamline at -14 degrees

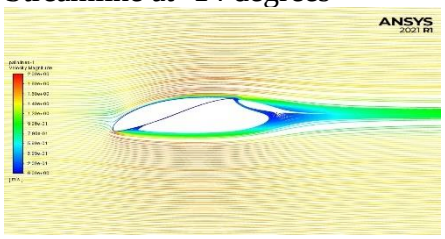

C_p contour at -12 degrees

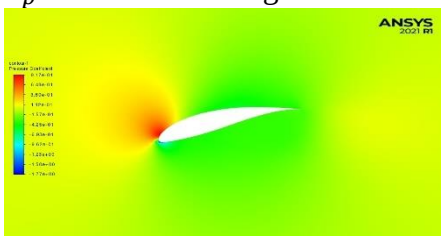

Streamline at -12 degrees

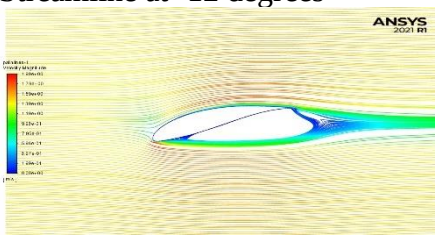

C_p contour at -10 degrees

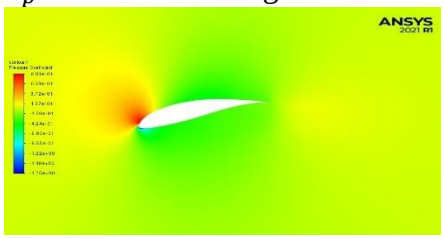

Streamline at -10 degrees

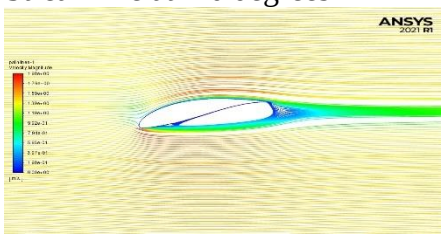

C_p contour at -8 degrees

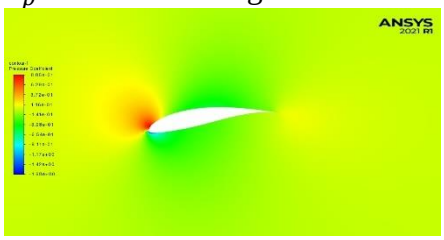

Streamline at -8 degrees

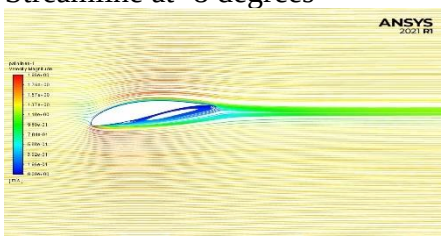

C_p contour at -6 degrees

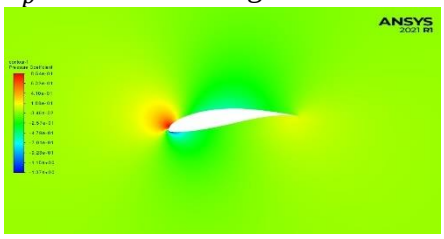

Streamline at -6 degrees

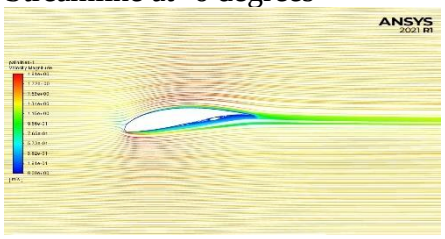

C_p contour at 0 degrees

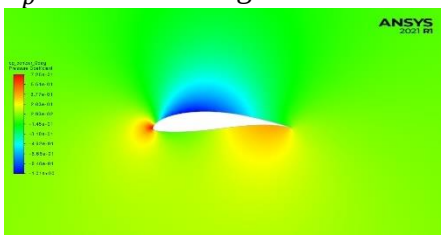

Streamline at 0 degrees

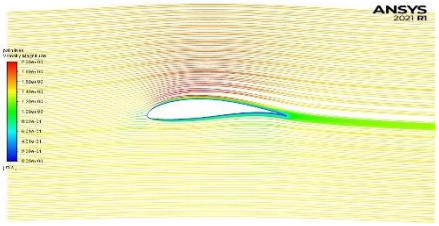

C_p contour at 6 degrees

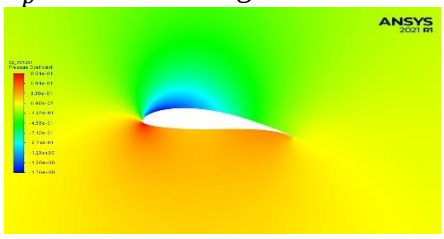

Streamline at 6 degrees

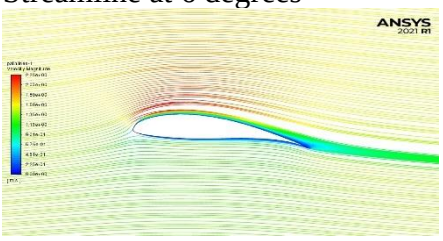

C_p contour at 8 degrees

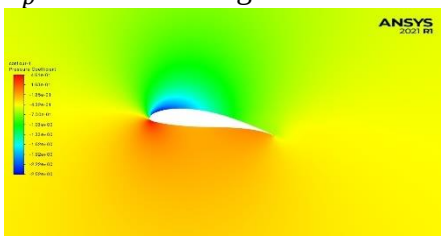

Streamline at 8 degrees

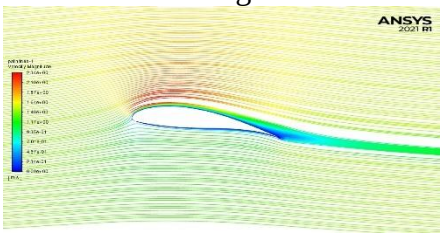

C_p contour at 10 degrees

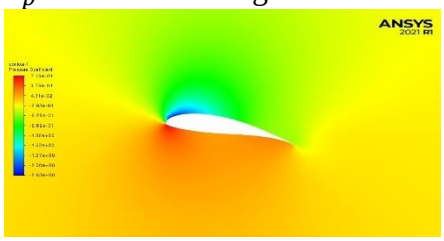

Streamline at 10 degrees

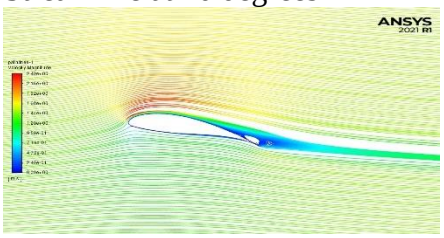

C_p contour at 12 degrees

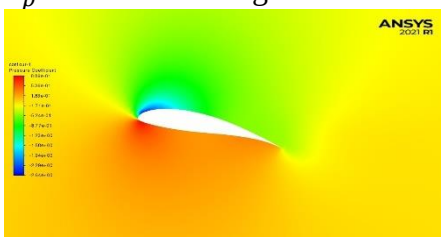

Streamline at 12 degrees

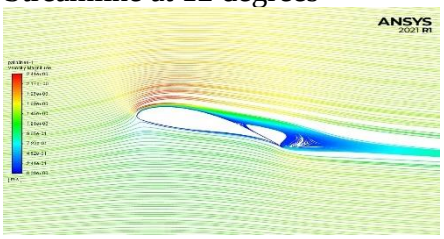

C_p contour at 14 degrees

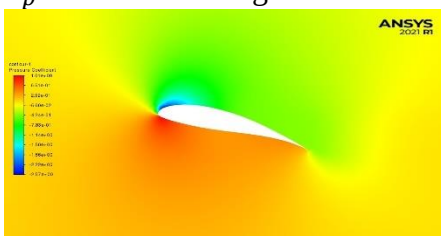

Streamline at 14 degrees

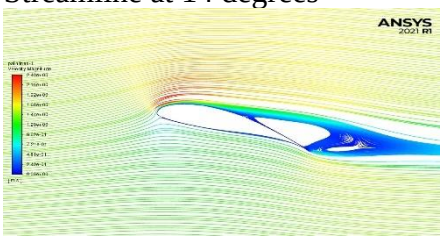

C_p contour at 16 degrees

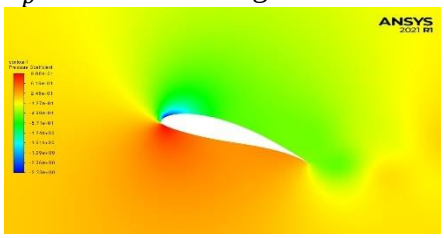

Streamline at 16 degrees

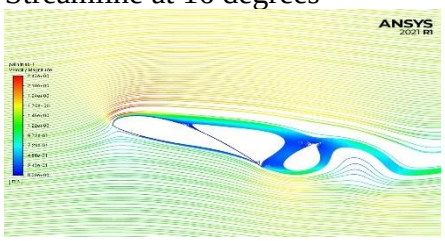

C_p contour at 18 degrees

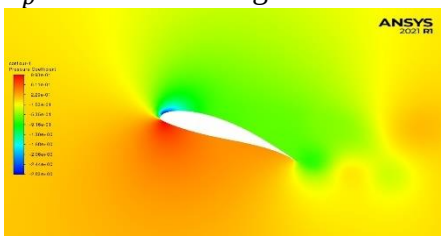

Streamline at 18 degrees

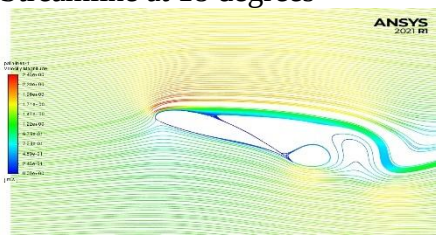

C_p contour at 20 degrees

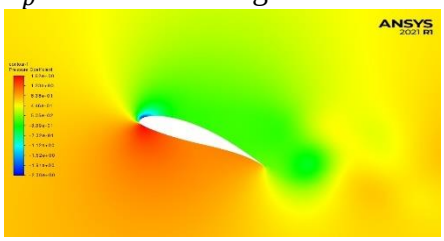

Streamline at 20 degrees

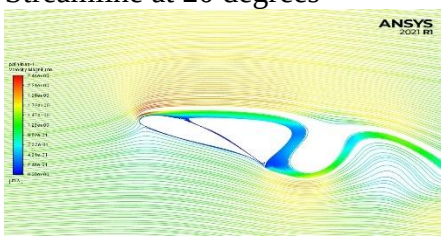

C_p contour at 22 degrees

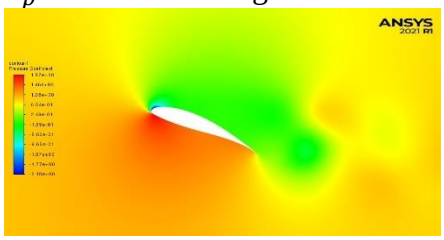

Streamline at 22 degrees

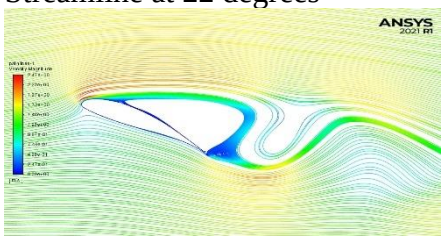

Note: The above table is a list of pressure coefficient contours and their equivalent streamlines. To save time only a few of the contours and streamlines are shown.

Note: The next table is a list of pressure coefficient as a function of chord length. To save time only a few of the contours are shown.

C_p vs Chord at -16 degrees

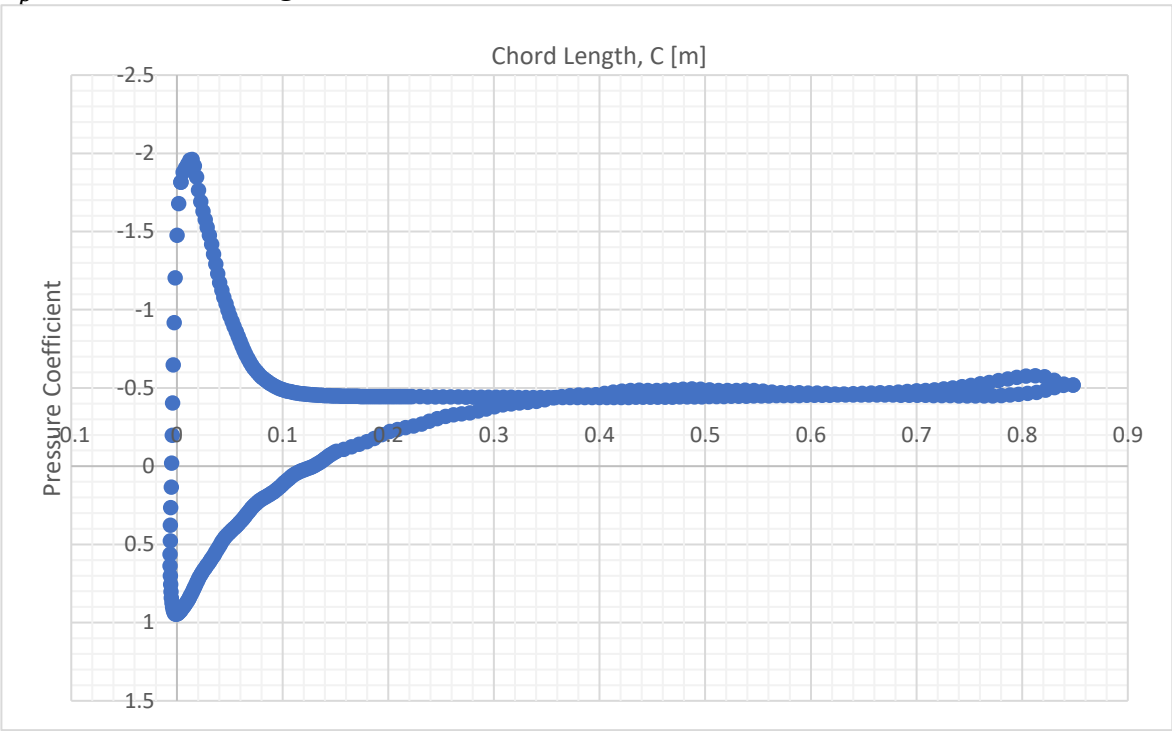

C_p vs Chord at -12 degrees

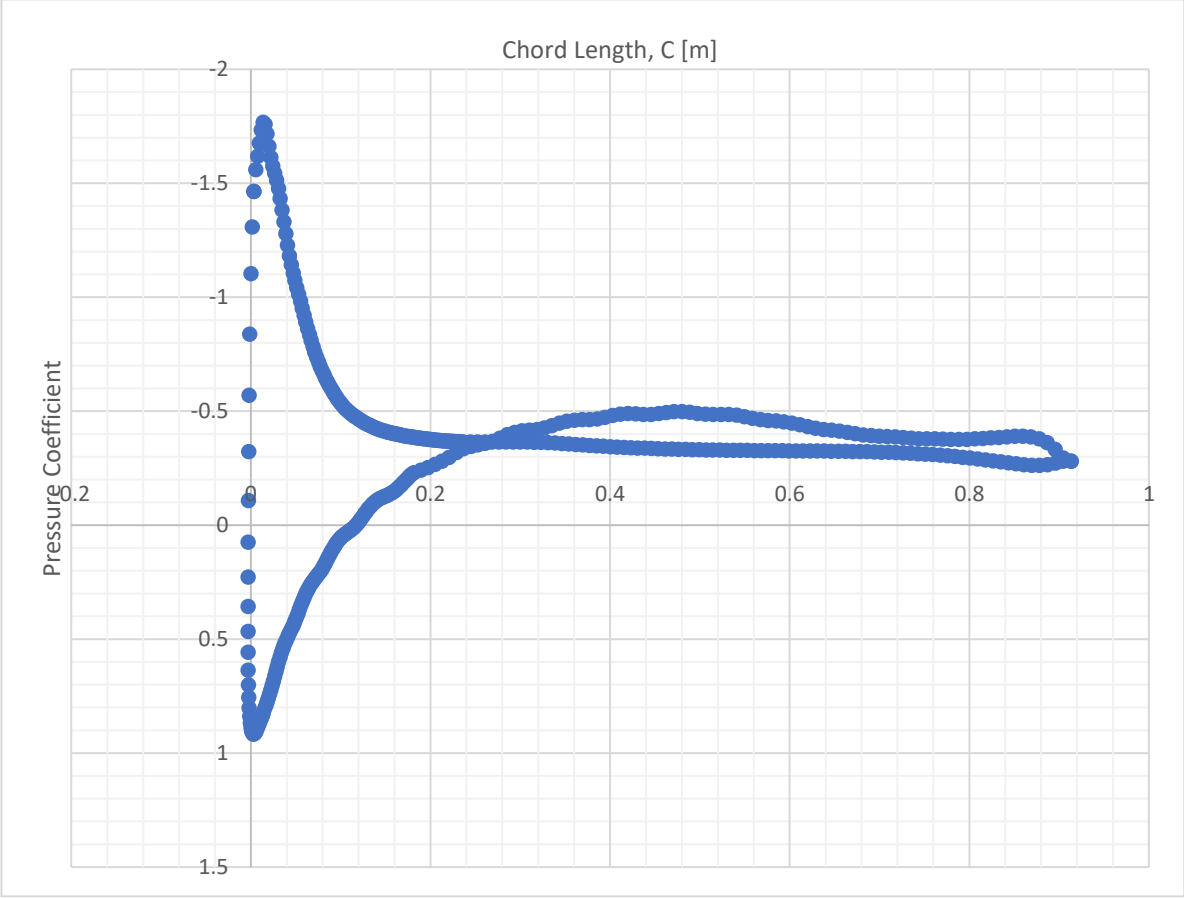

C_p vs Chord at -8 degrees

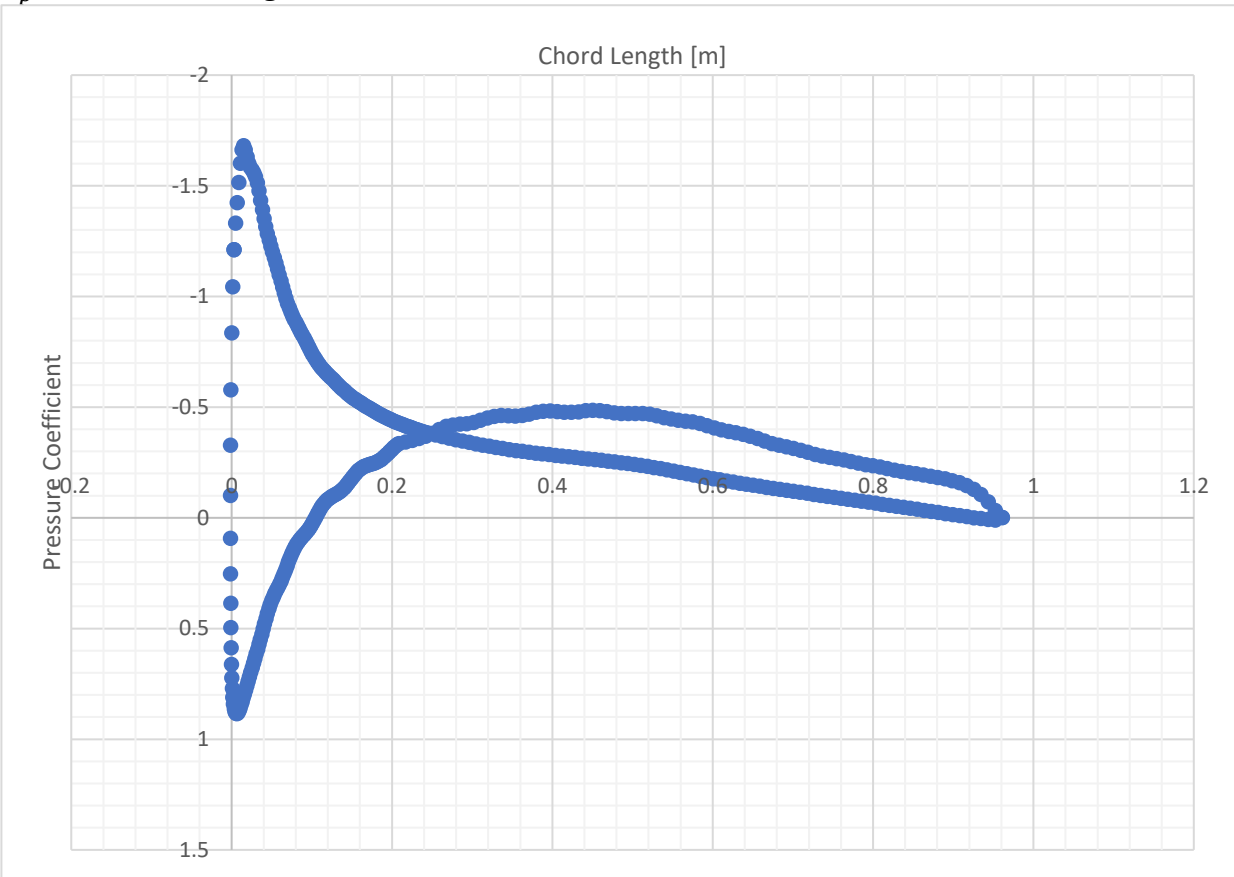

C_p vs Chord at 0 degrees

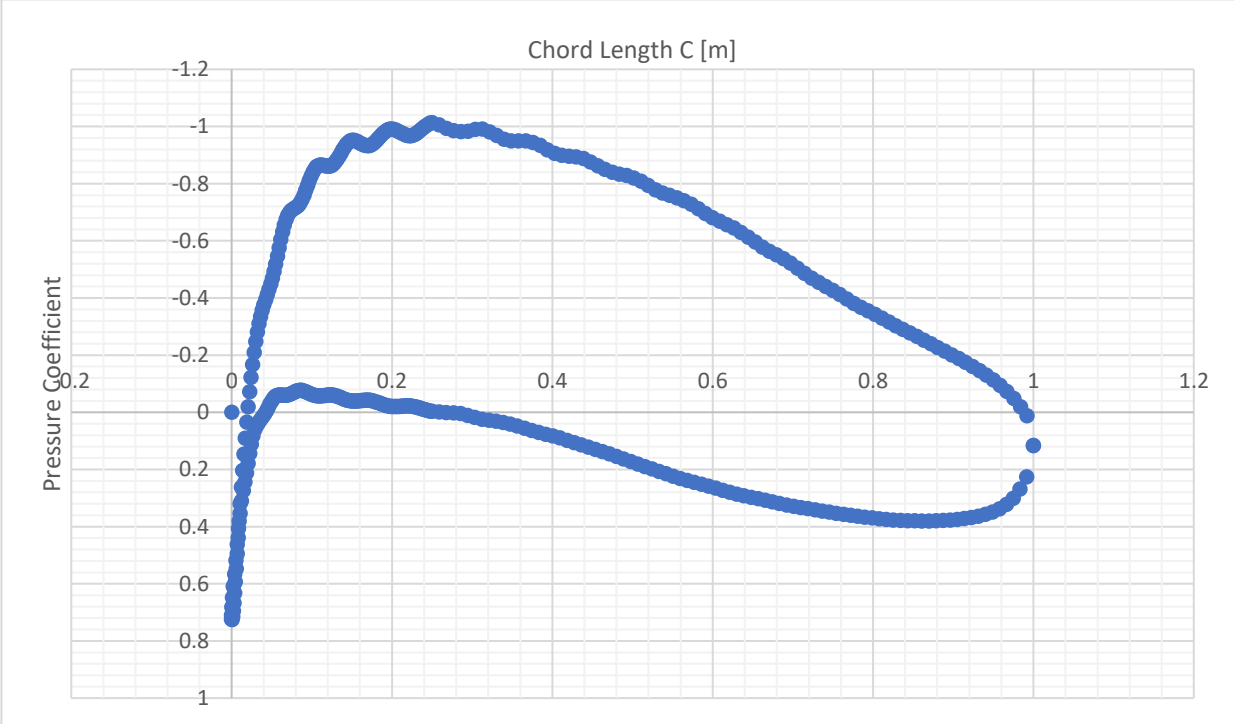

C_p vs Chord at 6 degrees

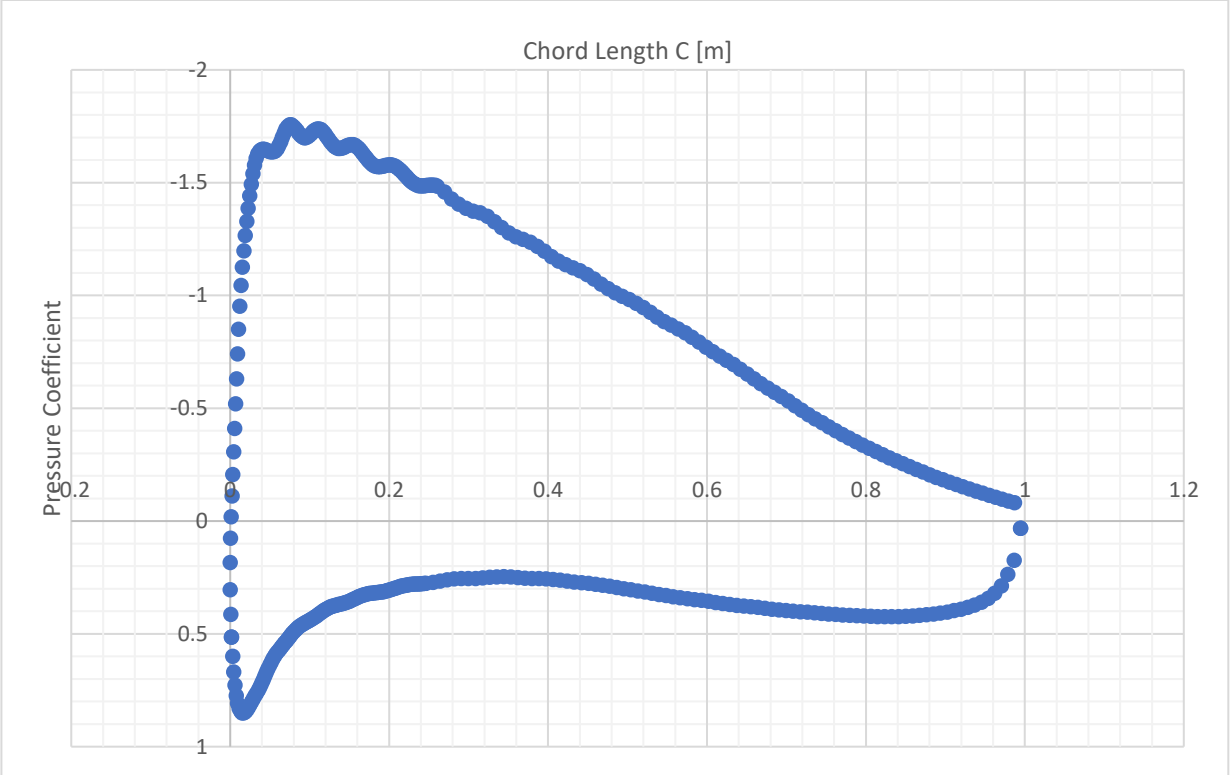

C_p vs Chord at 10 degrees

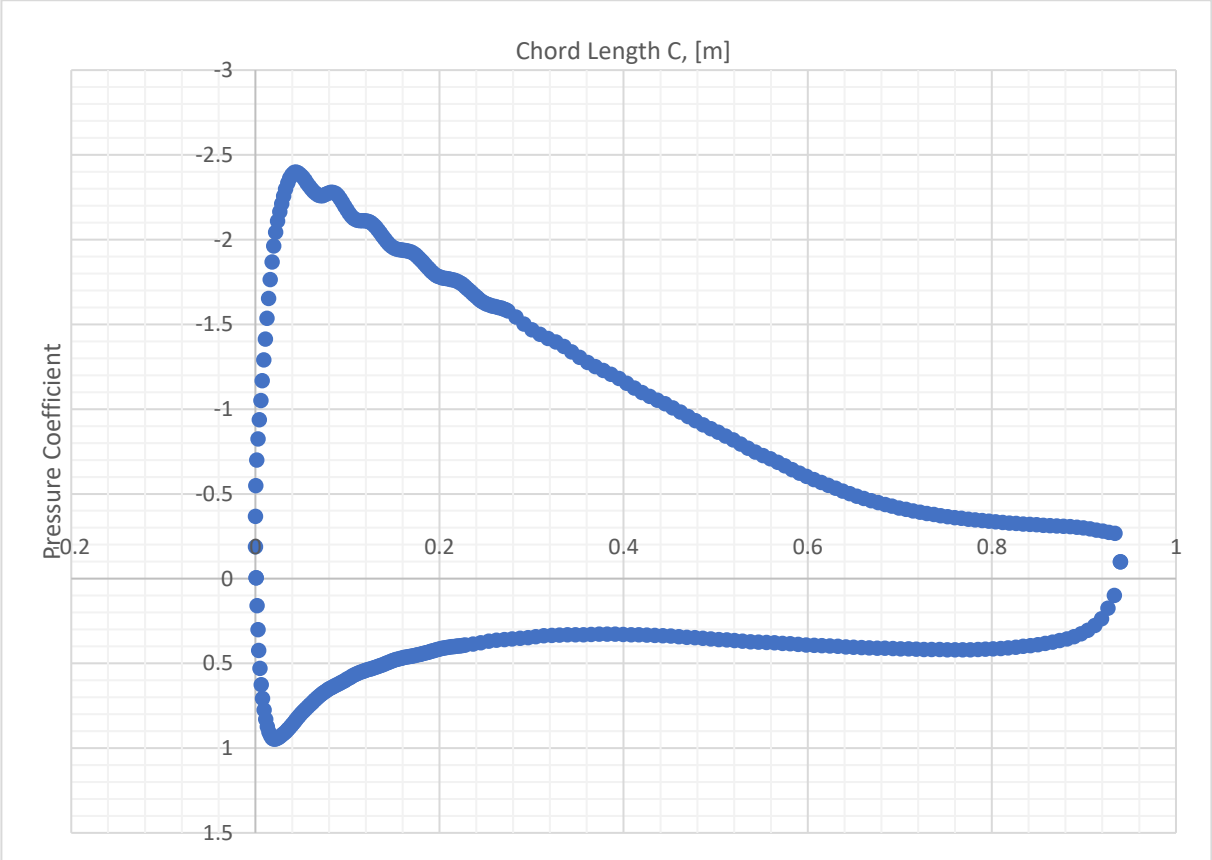

C_p vs Chord at 18 degrees

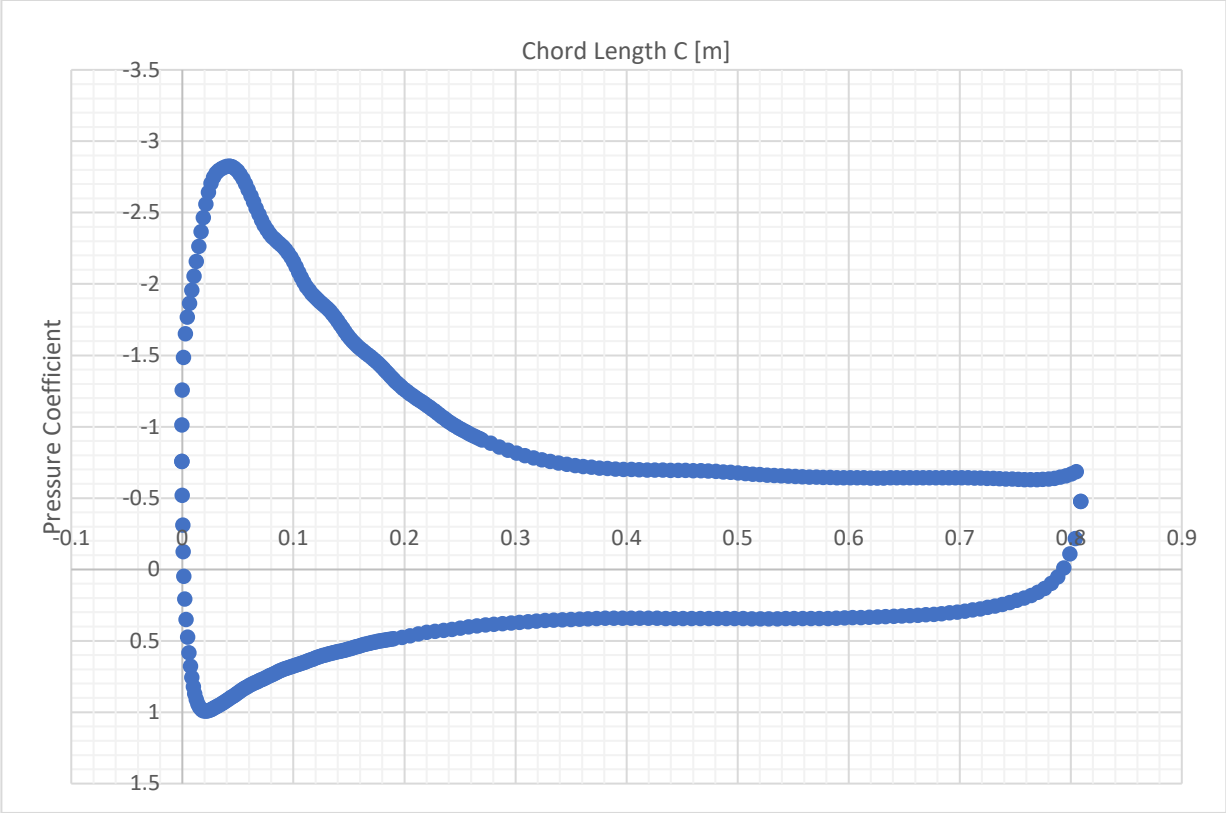

C_p vs Chord at 22 degrees